Atmosphere-Ocean

ISSN: 0705-5900 (Print) 1480-9214 (Online) Journal homepage: www.tandfonline.com/journals/tato20

Statistical Modes and Physical Drivers of Multidecadal Sea Surface Temperature Variability in the Northwest Atlantic

J. Coyne & E. Oliver

To cite this article: J. Coyne & E. Oliver (2025) Statistical Modes and Physical Drivers of Multidecadal Sea Surface Temperature Variability in the Northwest Atlantic, Atmosphere-Ocean, 63:4, 278-298, DOI: 10.1080/07055900.2025.2530439

To link to this article: https://doi.org/10.1080/07055900.2025.2530439

Statistical Modes and Physical Drivers of Multidecadal Sea Surface Temperature Variability in the Northwest Atlantic

J. Coyne * and E. Oliver

Department of Oceanography, Dalhousie University, 6299 South Street, Halifax, NS, Canada

[Original manuscript received 16 December 2024; accepted 24 June 2025]

ABSTRACT *Variations in ocean temperature and the presence of large multidecadal sea surface temperature (SST) oscillation can have a severe impact on Northwest Atlantic climate, ecosystems and fisheries. Differences between historical SST datasets in the regions have also been consistently noted. When determining patterns of variability in Northwest Atlantic SST, steps should be taken to consider cross-dataset variability. Here, a novel combined-dataset approach from 1901 to 2010 was used along with an extended empirical orthogonal function (EEOF) analysis to determine the leading modes of variability over the Northwest Atlantic shelf and slope. Second, a mixed-layer heat budget from 1850 to 2015 was used to determine the dominant physical processes driving yearly-to-multidecadal variability across the Northwest Atlantic shelf and slope. Results from the EEOF suggest that positive Atlantic Multidecadal Oscillation (AMO) years are driven by positive North Atlantic Oscillation years (NAO).*

RÉSUMÉ *[Traduit par la rédaction] Les variations de la température de l'océan et la présence d'une importante oscillation multidécennale de la température de surface de la mer (TSM) peuvent avoir une incidence considérable sur le climat, les écosystèmes et les pcheries de l'Atlantique Nord-Ouest. Des différences entre les ensembles de données historiques sur la TSM dans les régions ont également été observées de manière constante. Lors de la détermination des modèles de variabilité de la TSM dans l'Atlantique Nord-Ouest, des mesures doivent être prises pour prendre en compte la variabilité entre les ensembles de données. Ici, une nouvelle approche d'ensembles de données combinés de 1901 à 2010 a été utilisée avec une analyse de fonction orthogonale empirique étendue (FOEE) pour déterminer les principaux modes de variabilité sur le plateau et le talus de l'Atlantique Nord-Ouest. Deuxièmement, un bilan thermique de la couche mixte de 1850 à 2015 a servi à déterminer les processus physiques dominants à l'origine de la variabilité annuelle à multidécennale sur le plateau et le talus de l'Atlantique Nord-Ouest. Les résultats de la FOEE donnent à penser que les années d'oscillation atlantique multidécennale (OAM) positives sont entraînées par les années d'oscillation nord-atlantique (NAO) positives.*

KEYWORDS sea surface temperature; climate variability; mixed layer heat budget; climate modes

1 Introduction

Les variations de la température de l'océan et la présence d'une importante oscillation multidécennale de la température de surface de la mer (TSM) peuvent avoir une incidence considérable sur le climat, les écosystèmes et les pcheries de l'Atlantique Nord-Ouest. Des différences entre les ensembles de données historiques sur la TSM dans les régions ont également été observées de manière constante. Lors de la détermination des modèles de variabilité de la TSM dans l'Atlantique Nord-Ouest, des mesures doivent être prises pour prendre en compte la variabilité entre les ensembles de données. Ici, une nouvelle approche d'ensembles de données combinés de 1901 à 2010 a été utilisée avec une analyse de fonction orthogonale empirique étendue (FOEE) pour déterminer les principaux modes de variabilité sur le plateau et le talus de l'Atlantique Nord-Ouest. Deuxièmement, un bilan thermique de la couche mixte de 1850 à 2015 a servi à déterminer les processus physiques dominants à l'origine de la variabilité annuelle à multidécennale sur le plateau et le talus de l'Atlantique Nord-Ouest. Les résultats de la FOEE donnent à penser que les années d'oscillation atlantique multidécennale (OAM) positives sont entraînées par les années d'oscillation nord-atlantique (NAO) positives.

température de surface de la mer; variabilité climatique; bilan thermique de la couche mélangée; modes climatiques

Both warming trends and a large multidecadal oscillation have been identified in historical Northwest Atlantic sea surface temperature (SST) records (Loder & Wang, 2015, 2024; Petrie & Drinkwater, 1993), making the area especially susceptible to extreme SST events (Holbrook et al., 2019).

*Corresponding author's email: jonathan.coyne@dal.ca
Current affiliation: Oceanography, Fisheries and Oceans Canada, Newfoundland and Labrador Region, Canada

Given the historic and current climatic, cultural, and economic importance of the area, extreme SST events have the potential to have a large-scale coastal impact on local populations and ecosystems (e.g. Mills et al., 2013). This underlies the importance of understanding the physical forcing behind, as well as being able to predict, modes of SST variability.

Multidecadal oscillations in the Northwest Atlantic SST arise in part due to the general circulation of the region (Deser et al., 2010; Loder & Petrie, 1998; Loder & Wang, 2015, 2024; Petrie & Drinkwater, 1993). The Gulf Stream brings warm, relatively salty water up along the shelf towards Cape Hatteras (K. Chen et al., 2014; Z. Chen et al., 2020; Loder & Petrie, 1998), while the Labrador Current brings cool fresh water from the Arctic along the Northwest Atlantic Shelf down to the Scotian Shelf, and sometimes further south (Z. Chen et al., 2020; Han, 2003; Han et al., 2014; Loder & Petrie, 1998). The relative strength of both the Gulf Stream and Labrador Current changes over time resulting in significant changes to SST and SST anomaly (SSTA) (Deser et al., 2010; Han et al., 2014; Loder & Wang, 2015, 2024). These converging ocean boundary currents, along with sea level pressure anomalies, result in the Northwest Atlantic shelf and slope showing the highest interannual-to-multidecadal variability in the North Atlantic (Deser et al., 2010; Han et al., 2014; Petrie & Drinkwater, 1993). Climate modes have been used to define these potentially-predictable patterns of North Atlantic SST variability (Deser et al., 2010; Loder & Wang, 2015, 2024), with the two most relevant to the region being the Atlantic Multidecadal Oscillation (AMO) and North Atlantic Oscillation (NAO) (Deser et al., 2010; Loder & Wang, 2015, 2024). The combination of warming trends and large multidecadal oscillation makes the area especially susceptible to extreme SST events (Holbrook et al., 2019; Loder & Wang, 2015, 2024; Petrie & Drinkwater, 1993), while also underlining the importance of understanding and being able to predict Northwest Atlantic SST variability. Along with SST anomalies, strong NAO events also have impacts on remote regions, including the triggering and subsequent maintenance of an atmosphere wave train running from the North Atlantic to East Asia (S. Chen et al., 2020b, 2021), increases in southern ice export through the Fram Strait (Hilmer & Jung, 2000), and changes to precipitation levels over Europe (Vicente-Serrano & López-Moreno, 2008). Springtime tripolar SSTAs, typically associated with positive NAO years, can also impact Arctic sea ice concentration anomalies in the Greenland and Barents Seas which in turn may influence the following winter El Niño Southern Oscillation (S. Chen et al., 2024). Given the historic and current climatic and economic importance of the area, extreme SST events have the potential to have a large-scale impact on local populations and ecosystems (Mills et al., 2013; Oliver et al., 2021).

The AMO is a large-scale climate mode exhibiting multidecadal variability in SST on timescales of 60–70 years (Deser et al., 2010; Loder & Wang, 2015). Positive (negative) AMO years are associated with a positive (negative) SSTA pole located in the middle of the North Atlantic (Deser et al., 2010; Loder & Wang, 2015, 2024; Wills et al., 2019). Positive AMO years may occur as the result of consistent negative air-sea heat flux over the Labrador Sea driving Atlantic Meridional Overturning Circulation to advect warm water north (Wills et al., 2019). This leads to anomalously warm ocean temperatures throughout the Atlantic and the formation of a low pressure cell. With time, the Atlantic Meridional Overturning Circulation over-corrects the initial cold water scenario leading to increased stratification in the Labrador Sea. This weakens the Atlantic Meridional Overturning Circulation and causes the dissipation of the positive AMO event. It should be noted that the physical forcings behind the AMO are still debated (Deser et al., 2010; Loder & Wang, 2015). This is partially due to the long timescale on which the AMO oscillates and the corresponding lack of available data. Given that many of the oceanic/atmospheric variables needed to determine the forcing behind AMO changes are not observed over many AMO cycles (if any), this makes the analysis of potential forcing difficult.

The NAO represents changes in sea level pressure between the Arctic and the Atlantic subtropics forced by the redistribution of atmospheric mass (Deser et al., 2010; Marshall et al., 2001; Visbeck et al., 2003). The effect of the positive NAO on North Atlantic SSTA is characterized as a tripolar structure, with negative anomalies in the subpolar North Atlantic and subtropics, and positive anomalies in the mid-latitudes (the opposite pattern occurs during negative NAO years) (Deser et al., 2010; Loder & Wang, 2015, 2024). The combined latent and sensible heat flux mirrors this tripolar structure and so the ocean loses heat energy to the atmosphere in the subpolar North Atlantic (Deser et al., 2010). This is the result of the changes in sea level pressure, which during positive index years results in a strengthened Iceland low pressure cell and Azores high pressure cell. The strengthening of the pressure cells results in anomalously strong westerlies and northeast trade winds. Meanwhile, at mid-latitudes the ocean gains heat energy from the atmosphere as a result of weakened westerlies and enhanced warm air advection along the Eastern United States. Anomalous wind speeds and the resulting Ekman transport can also strengthen the Gulf Stream and Labrador Current during positive years (Deser et al., 2010). Additionally, the anomalous wind speeds associated with NAO results in modulating surface heat fluxes which further reinforce the tripolar pattern (S. Chen et al., 2020a), mainly through variations in sensible and latent heat flux (Deser et al., 2010). It is also important to note that the relationship between NAO and North Atlantic SSTA is not stable.

Compared to most other areas of the world, the Northwest Atlantic shelf and slope have a relatively high number of SST observations going back over 150 years (Deser et al., 2010; Kent et al., 2021), allowing for the creation of observation-based global gridded data products. Differences amongst global gridded data products have been noted in the past resulting from data sparcity, interpolation methods, and

corrections to the source data (Deser et al., 2010; Loder & Wang, 2015, 2024). Historically, modes of variability in the Northwest Atlantic have been defined from a single data product, commonly by performing an empirical orthogonal function (EOF) analysis, and do not consider cross-dataset variability or consistency (Loder & Wang, 2015, 2024). Interpretation of EOF results is also often done by correlating the resulting principal components (PCs) time series with known climate modes (e.g. AMO, NAO) (Loder & Wang, 2015, 2024). This makes it difficult to relate EOF results to specific oceanic and atmospheric variables in the region as the statistics do not necessarily correspond to the physics. Loder and Wang (2015, 2024) found significant correlation between the leading two modes of a North Atlantic SSTA EOF analysis with AMO and NAO (corresponding to the first and second mode respectively). Along with AMO and NAO, other climate modes have been noted to have an impact on North Atlantic SSTA, including El Niño Southern Oscillation (Deser et al., 2010) and Pacific Decadal Oscillation (Enfield et al., 2001). Past decompositions of North Atlantic SSTA show that the AMO and NAO together dominate SSTA variability in the region (Loder & Wang, 2015, 2024). This justifies the focus of this study on AMO and NAO alone; analysis will not be conducted on other climate models.

In this paper, modes of SSTA variability along the Northwest Atlantic shelf and slope were determined with the aim to better understand the amplitude and phasing of yearly-to-multidecadal variability and its physical drivers and its relationship to regional circulation and the role of the AMO and NAO. In Section 2 we summarize the data products/climate model output used in the paper along with the relevant methods. In Section 3 we use a novel, multi-dataset approach to determine the role and possible drivers of yearly to multidecadal variability in Northwest Atlantic shelf and slope SST. In Section 4 we use a global climate model to create a mixed layer temperature heat budget of the Northwest Atlantic shelf and slope regions from 1850 to 2015. A discussion of our findings is presented in Section 5.

2 Data and methods

a *Global Gridded Data Products and Climate Model Output*

Monthly SST was obtained from five observation-based datasets. HadISST V1.1 (Rayner et al., 2003), ERSST V5 (Huang et al., 2017), and COBE SST (Hirahara et al., 2014) use historical SST measurements and statistical interpolation methods to create spatially and temporally complete observation-based datasets. CERA-20C (Laloyaux et al., 2018, no longer publicly available as of 2023) and SODA (Giese et al., 2016) are both ocean re-analysis datasets which combine numerical ocean models with historical SST recordings, via data assimilation, to create a spatially and temporally complete observation-based datasets. Differences have been noted in past literature when comparing in-situ SST measurements with satellite-derived SST (O'Carroll et al., 2008) as is done here. For the purposes of this paper, no additional corrections will be done to make these diverse datasets more consistent. Additional ocean/atmospheric variables were taken from SODA and CERA-20C including net air-sea heat flux (the sum of shortwave radiation, longwave radiation, sensible heat flux, and latent heat flux) and net fresh water flux (the sum of evaporation and precipitation).

Model output was used from the CESM2-LENS global climate model which was developed to examine climate sensitivity to anthropogenically-forced global warming (Rodgers et al., 2021). CESM2-LENS was selected for its ability to accurately reproduce oceanographic and atmospheric circulation, making it an ideal choice for studying climate change and natural variability (Rodgers et al., 2021; Simpson et al., 2020). Simpson et al. (2020) found that CESM2-LENS accurately represented the NAO sea level pressure structure well, especially during winter and summer months, but also noted there was a large sampling uncertainty across ensemble members. Less literature is available studying CESM2-LENS ability to accurately reproduce the AMO climate index's SST structure. We address this knowledge gap in Section a. The downloaded output of the CESM2-LENS (1850–2015) is subject to historical records of anthropogenic and natural forcing (Rodgers et al., 2021). The ocean and atmosphere outputs are from the Parallel Ocean Program version 2 and have a non-constant spatial resolution of approximately 1° latitude by 1° longitude with latitude grid spacing increasing towards the poles. Here, we use ten of the macro-initialization ensemble members due to lack of data availability at the time of this study; 1001, 1021, 1041, 1061, 1081, 1101, 1121, 1141, 1161, and 1181. The following monthly ocean/atmospheric variables were obtained from the CESM2-LENS output; temperature tendency ($\frac{\partial T}{\partial t}$), mixed layer depth (MLD, h), advective flux of heat in the grid-x, y, and z directions ($\nabla \cdot (\vec{v}T)$), total surface heat flux (Q_{mdSHF}), solar shortwave heat flux (Q_{mdSW}), temperature flux across the bottom face from diabatic implicit vertical mixing, sensible heat flux (Q_{mdsen}), upwards longwave heat flux and downwards longwave heat flux (sum to Q_{mdLW}), and finally the heat flux due to the latent heat of evaporation, melt, snow, and ice runoff (summed to the latent heat flux, *Qmdlat*). MLD is defined as the shallowest depth where the local buoyancy gradient is at its maximum (Large et al., 1997).

The observed monthly AMO index (1870 to 2015) and NAO index (1865 to 2019) was obtained from Trenberth and Shea (2006) and Hurrell et al. (2003) respectively. Both the AMO and NAO were averaged to annual means.

b *Atlantic Multidecadal Oscillation and North Atlantic Oscillation*

In addition to observed AMO and NAO indices, indices from the CESM2 climate model were calculated as well. SSTA from the North Atlantic between the equator and 60°N was spatially averaged, and then smoothed with a 10-year running average. The global mean SSTA, between 60°N and 60°S, was then subtracted from the smoothed Atlantic

SSTA to find the AMO index. The AMO index was derived following the methods of Trenberth and Shea (2006).

The CESM2 NAO index was derived from finding the differences in sea level pressure between Lisbon, Portugal (64.148°N and 21.935°W, representing the Azores high) and Reykjavik, Iceland (38.685°N and 9.255°W, represents the Iceland low), following Hurrell et al. (2003).

c *Decomposition of Sea Surface Temperature*

SST can be considered the sum of three components:

$$T(t) = T^{Tr}(t) + T^{s}(t) + T'(t) \quad (1)$$

where $T(t)$ is the SST at time t, $T^{Tr}(t)$ is the linear SST trend at time t, $T^{s}(t)$ is the SST seasonal cycle (climatology) at time t, and $T^{'}(t)$ is the SSTA at time t. The linear SST trend, $T^{Tr}(t)$, was calculated by least square regression over the entire SST time period. The climatology, $T^{s}(t)$, calculated by finding the mean SST for each month from 1920 to 1950 (Loder & Wang, 2015), was then subtracted from the SST for all datasets to find the SSTA with long term trend, $T^{Tr}(t) + T'(t)$. For datasets with multiple ensemble members, the ensemble mean and standard deviation was calculated after the climatology was removed. After the climatology had been calculated and removed, monthly SSTA was temporally averaged to yearly SSTA. The same decomposition was performed on the CESM2-LENS oceanic/atmospheric variables including temperature tendency.

d *Regions of Interest*

In order to determine the meridional and temporal structure of SSTA and mixed layer temperature tendency anomaly in the Northwest Atlantic shelf and slope region, specific regions of interest were defined using local bathymetry following

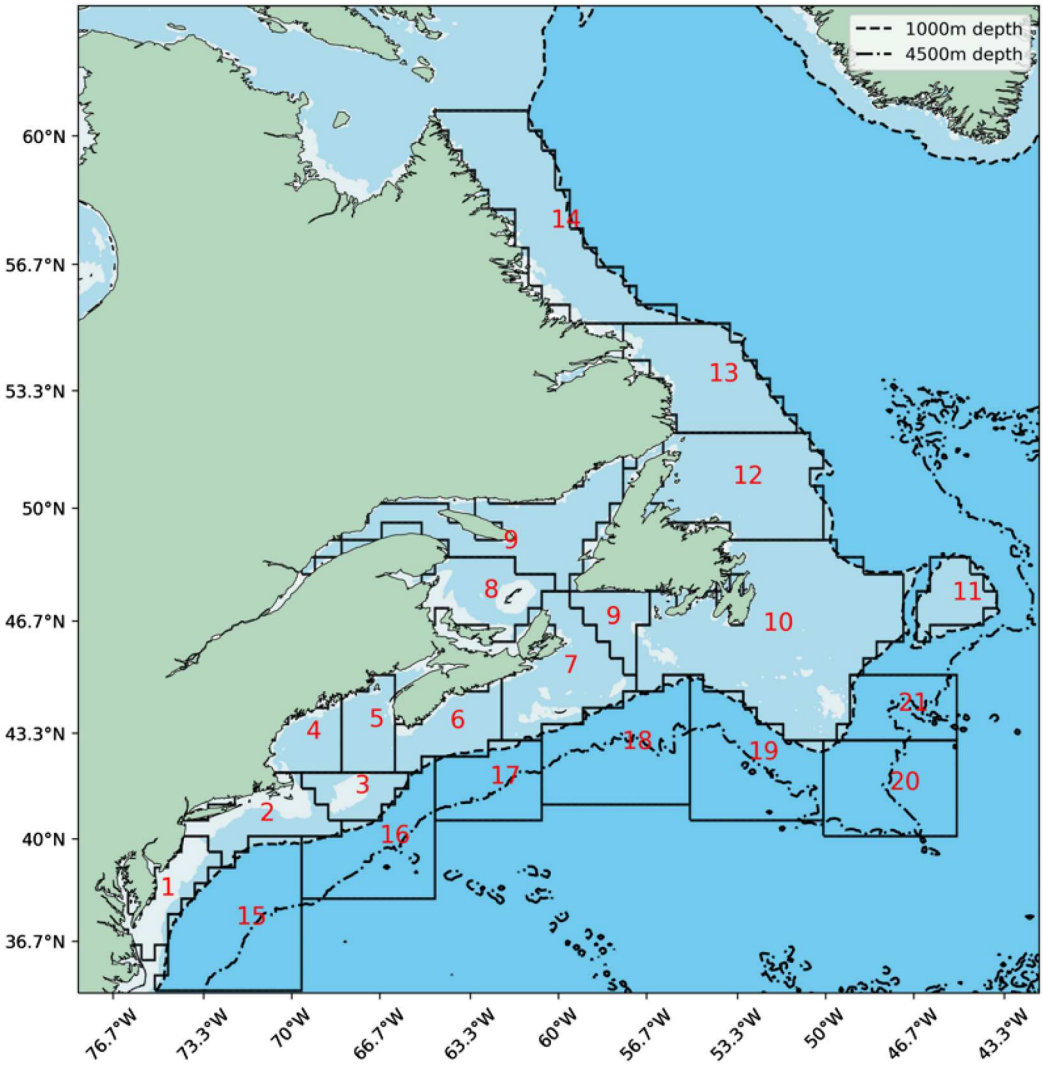

Fig. 1 Northwest Atlantic shelf and slope regions of interest on top of local bathymetry. Regions are outlined by solid black lines, 1000 metres depth is given by the dashed line, 4500 metres depth is given by the dash dot line. Specific regions are numbered from 1 to 21 in red with 1 to 14 being shelf regions and 15 to 21 being slope regions. The area south of Western Newfoundland, is part of region 9.

Richaud et al. (2016) and Z. Chen et al. (2020). The regions extend meridionally from Cape Hatteras, North Carolina, to Cape Chidley, Labrador (Fig. 1). Regions 1–14 correspond to the Northwest Atlantic shelf (0–1000 m depth). Regions 1–3 are associated with the Mid-Atlantic Bight, 4–5 with the Gulf of Maine, 6–7 with the Scotian Shelf, 8–9 with the Gulf of St. Lawrence, 10–11 with the Grand Banks and Flemish Cap, and 12–14 with the Northern Newfoundland Coast and Labrador Shelf. Regions 15-21 correspond to the Northwest Atlantic slope (4000 m+ depth) and are restricted to be south of 45°N as slope waters along the Labrador Shelf are difficult to define (Z. Chen et al., 2020). The slope regions also follow the general path of the Gulf Stream. The regional average SSTA was then calculated for each of the global gridded data products and CESM2-LENS oceanic/atmospheric variables.

e *Empirical Orthogonal Functions*

An EOF analysis is a statistical method in which a dataset (varying in space and time) is decomposed into a set of statistical modes, consisting of uncorrelated simultaneous time series' (PC) and accompanying spatial patterns (EOF pattern). The percentage of total variance, R_i^2, that a mode represents can be found by dividing its associated eigenvalue, λ_i, by the sum of all eigenvalues and multiplied by 100,

$$R_i^2 = \frac{\lambda_i}{\sum_i \lambda_i} \times 100\%. \tag{2}$$

The largest eigenvalue corresponds to the mode that explains the most variability. The standard EOF analysis (e.g. Deser et al., 2010; Loder & Wang, 2015, 2024) is for a single dataset e.g. a single record of temperature at each spatial location. In order to perform an EOF analysis on a combined dataset where multiple records of temperature exist for each location, an EEOF approach was taken. Regionally-averaged SSTA from each region of interest (Fig. 1), with the linear trend removed, were calculated for each of the observation-based datasets according to a climatology from 1920 to 1950.

The combined dataset, T, can be written as

$$T(r, d, t) = [T1(r, t) \quad T2(r, t) \quad T3(r, t) \quad T4(r, t) \quad T5(r, t)], \tag{3}$$

consisting of a concatenated array of five different temperature datasets, $T1, T2, \ldots T5$, where r is the region, d is dataset number ($d = 1, 2, \ldots 5$), and t is time. Prior to the EEOF analysis, the detrended SSTA was also scaled by the area of the gridcell to account for the changing area between the regions of interest and the non-constant spacing in latitude; this has the additional effect of weighing each dataset equally. An EEOF was then calculated on this array from January 1901 to December 2010, with the output being rescaled by the grid cell area. This analysis provides one PC time series and five EOF spatial patterns for each mode. The PC for each mode is divided by, and the EOF patterns for that mode are multipled by, the standard deviation of the associated PC so that the PCs are normalized to have a standard deviation of 1. All of the EOF modes can then be interpreted in units of °C, assuming a PC value of order 1.

In order to determine whether each mode's explained variance is greater than random noise, modes generated from random data were compared to our results (also known as the Monte Carlo method; Overland & Preisendorfer, 1982). Covariance matrices and eigenvalues are determined for randomly generated arrays with a mean of 0 and unit variance. The eigenvalues are then divided by the total sum of eigenvalues in order to determine the percentage of explained variance. This process is then repeated 100 times. All percentages corresponding to the first mode across the 100 randomly generated arrays are then sorted from greatest to least. The same process is done for all remaining modes. The percentages resulting from the actual data products were then divided by the 95th highest percentage of the same mode in the randomly generated arrays. This is known as the Rule N (Overland & Preisendorfer, 1982),

$$\text{Rule } N = \frac{R_{r,i}^2}{R_{N95,i}^2}, \tag{4}$$

where R^2 is the percentage of explained variance, r refers to the real mode derived from the SSTA datasets, N refers to modes derived from generated noise, and i represents the mode of interest. The superscript 95 represents the 95th highest explained variance corresponding to a specific mode, i. Modes with Rule N values higher than 1 are considered significant and modes with Rule N values below 1 are considered indistinguishable from eigenvalues generated from noise.

It is important that the EEOF results have uncertainty estimates in time and space. The five EOF patterns correspond to each of the observation-based datasets. The ith space-time temperature pattern T_i can be written as

$$T_i(r, d, t) = p_i(r, d)u_i(t), \tag{5}$$

where T_i is the SSTA mode of variability, p_i is the EOF pattern, and u_i is the PC time series. A dataset-mean ($\overline{p_i}(r)$) and standard deviation ($\sigma_p(r)$) EOF pattern was found by spatially interpolating each of the EOF patterns to the common highest resolution and calculating the mean and standard deviation across the EOF patterns.

In order to convert the standard deviation in the EOF pattern to a standard deviation in the PC time series, the following method was used. If we rewrite the EOF pattern (p_i) as the sum of the mean pattern ($\overline{p_i}$) +/− the standard deviation (σ_{p_i}), then the uncertainty in $T_i(r, d, t)$, expressed as a standard deviation denoted $\sigma_{T_i}(r, d, t)$, can be determined using the following equation,

$$T_i(r, d, t) \pm \sigma_{T_i}(r, d, t) = (\overline{p_i}(r, d) \pm \sigma_{p_i}(r, d))u_i(t), \tag{6}$$

where $\sigma(\cdot)$ and $\bar{\cdot}$ are the standard deviation and the mean of the variable, respectively across all d (datasets). I follow this with a series of algebraic manipulations to determine a PC time

series uncertainty σ_{u_i},

$$T_i(r, d, t) \pm \sigma_{T_i}(r, d, t) = \overline{p_i}(r, d)u_i(t) \pm \sigma_{p_i}(r, d)u_i(t) \quad (7)$$

$$= \overline{p_i}(r, d)\left(u_i(t) \pm \frac{\sigma_{p_i}(r, d)u_i(t)}{\overline{p_i}(r, d)}\right) \quad (8)$$

$$= \overline{p_i}(r, d)(u_i(t) \pm \sigma_{u_i}(t)), \quad (9)$$

where the standard deviation of the PC time series $\sigma_{u_i}(t)$ is given by

$$\sigma_{u_i}(t) = \frac{\sigma_{p_i}(r, d)u_i(t)}{\overline{p_i}(r, d)}. \quad (10)$$

This now provides a measure of uncertainty, arising from inter-dataset differences, on the PC time series $u_i(t)$.

In the previous section, an EEOF was used to allow for the analysis of multiple observation-derived SST data products. Due to how the initial conditions are defined for CESM2-LENS ensemble members, namely that initial conditions are taken every ten years from a natural control run and therefore do not have constant phasing across ensemble members, it was found that the use of an EEOF was not practical for determining modes of variability from CESM2-LENS output. It was also found that temperature tendency time series are noisier than the temperature time series they are derived from. This makes the use of an EEOF even more impractical as the high noise levels make it harder to define common modes of variability across multiple ensemble members. For these two reasons, we have decided to instead use a standard EOF rather than an EEOF for the CESM2-LENS output. As a result of using temperature tendency from CESM2, the cumulative sum of the PC time series (CPC) must be determined in order to compare the results to the observed time series.

f *Surface Mixed Layer Heat Budget*

A heat budget can be used to determine the underlying physical forcings behind changes in ocean temperature tendency (Shearman & Lentz, 2010; Stevenson & Niiler, 1983). A volume-averaged surface mixed layer heat budget is derived from conservation of heat and conservation of mass equations (Roemmich et al., 2005; Stevenson & Niiler, 1983).

Using the CESM2-LENS model output, a mixed layer temperature tendency anomaly heat budget was calculated using (Moisan & Niiler, 1998),

$$\begin{aligned}\underbrace{\frac{\partial \overline{T}}{\partial t}}_{\text{Temperature tendency}} &= \underbrace{-\overline{\mathbf{u}} \cdot \nabla_H \overline{T}}_{\text{Horizontal advection}} \underbrace{-\frac{\overline{T} - T_{-h}}{h} w_{-h}}_{\text{Vertical advection}} \\ &+ \underbrace{\frac{Q_{\text{mdSHF}}}{\rho C_p h}}_{\text{Air-sea heat flux}} \underbrace{-\frac{1}{h} k_z \frac{\partial T}{\partial z_{-h}}}_{\text{Vertical Mixing}} \\ &+ \underbrace{\overline{\nabla_H \cdot (kmd_h \nabla_H T)}}_{\text{Horizontal mixing}} \underbrace{-\frac{\overline{T} - T_{-h}}{h}\left(\frac{\partial h}{\partial t} + \vec{u}_{-h} \cdot \nabla_H h\right)}_{\text{MLD tendency and lateral induction}},\end{aligned} \quad (11)$$

where an overbar here represents a vertical average over the mixed layer, $\overline{T}$ is the surface mixed layer temperature, t is time, $\mathbf{u}$ is horizontal velocity, ∇_H is the horizontal gradient operator, Q_{mdSHF} is the total surface heat flux, ρ is the seawater density, C_p is the specific heat capacity of seawater ($\rho C_p = 2.439 \times 10^7\ \text{Jm}^{-3\circ}\,\text{C}^{-1}$), h is the MLD, k_z is the vertical diffusivity coefficient, and k_{mdh} is the horizontal diffusivity coefficient. The total surface heat flux was calculated as the sum of five individual heat flux components,

$$Q_{\text{mdSHF=QmdSW}_0\text{-QmdSW}_{-h}\text{+QmdLW+Qmdsen+Qmdlat}} \quad (12)$$

where Q_{mdSW_0} is the surface shortwave heat flux, $Q_{\text{mdSW}}-h$ is the shortwave heat flux at the MLD, Q_{mdLW} is the longwave heat flux, $Q_{\text{mdsen)}}$ is the sensible heat flux, and Q_{mdlat} is the latent heat flux. Each term was vertically averaged over the MLD, shown here by $\bar{\cdot} = \frac{1}{h}\int_{-h}^{0} \cdot \text{mddz}$; $\cdot_{-h}$ indicates a variable taken at $-h$.

Horizontal diffusion was determined by finding the sum of eddy-induced advective temperature tendency, Redi temperature tendency, Robert filter temperature tendency, and submeso advective temperature tendency (Rodgers et al., 2021). A residual was determined by subtracting the horizontal advection, vertical advection, air-sea heat flux, and horizontal diffusion from the temperature tendency. The vertical mixing terms from the CESM2-LENS output only accounts for the air-sea heat flux input at the surface. In theory, the heat budget residual represents the vertical mixing not associated with air-sea heat flux. In practice, it also includes model and numerical error.

The volume average of each term (being a horizontal spatial average of the already vertically averaged terms) was determined for each of the predefined regions. The detrended anomaly of each heat budget term was determined by subtracting a 1920 to 1950 climatology and removing the linear trend over the entire time series of each term.

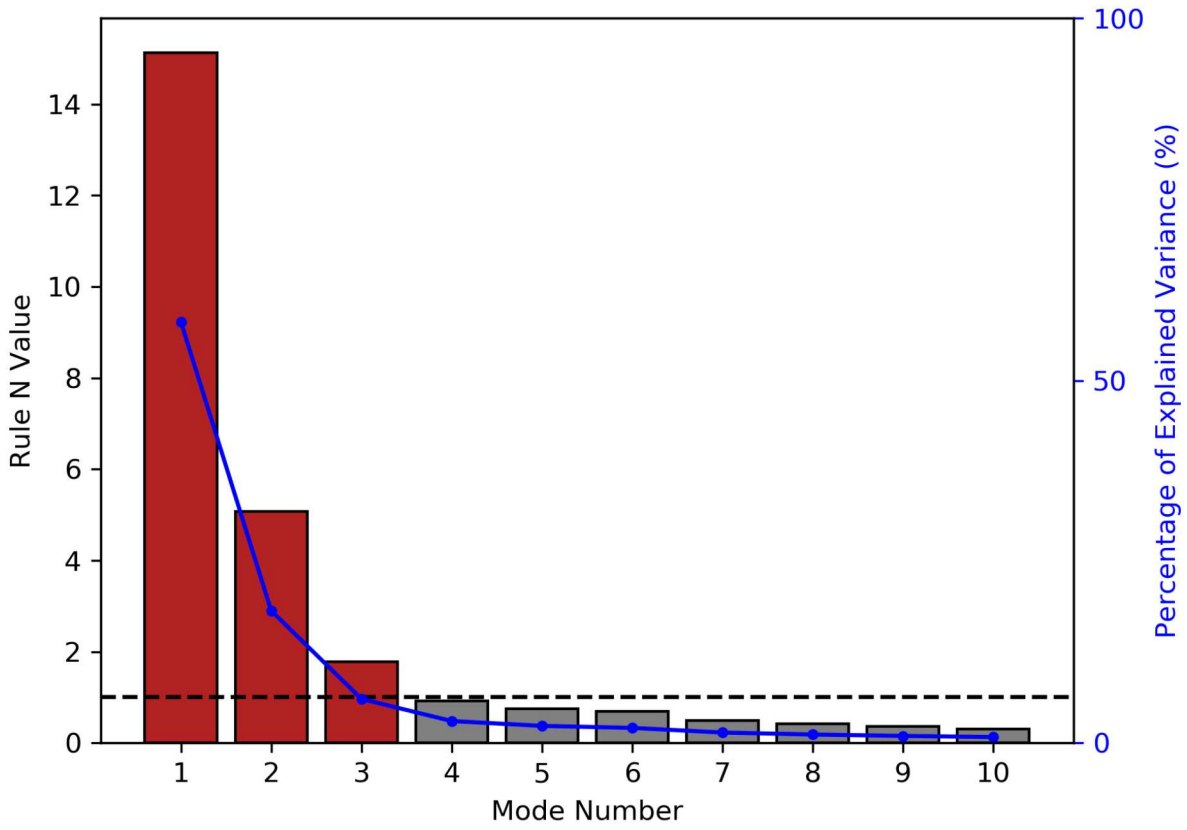

Fig. 2 EEOF mode significance for the first ten modes using the methods derived by Overland and Preisendorfer (1982). The threshold of 1 for the Rule N determines significance in the first ten modes (*dashed black line*). Modes that are significant are coloured red and modes that are insignificant are coloured grey. The percentage of explained variance for the first ten modes is also shown (*blue line*).

3 EEOF patterns and time series

a *Dominant Spatio-Temporal Patterns*

An EEOF was performed on detrended regionally-averaged SSTA from each of the observation-based datasets between 1901 and 2010. Using the method derived by Overland and Preisendorfer (1982), the first three EEOF modes were found to be significant (Fig. 2). Modes one through three explain 58.08%, 18.24%, and 6.07% respectively; collectively explaining 82.39% (Fig. 2).

Results from the multi-dataset EEOF show similar EOF patterns across data products for each mode. Differences between the EOF patterns occur in the magnitude of the poles with ERSST showing the highest magnitude EOF consistently through the first three modes. The spatial correlation coefficient across datasets was calculated for each mode. EEOF modes one through three had a correlation coefficient range of 0.87–0.97, 0.93–0.98, and 0.77–0.98 respectively. This gives us confidence to combine the EOFs across datasets. The EOF patterns were combined: the EOF pattern mean and standard deviation were determined (Eq. (6)) and the PC standard deviation was determined (Eq. (10)) (Fig. 3).

EOF pattern 1 mean (Fig. 3, first row) has a positive sign throughout the area of interest with a positive pole located east of Newfoundland (regions 10, 11, 21) with a maximum of 0.54°C. The mode decays to the north and south, over the Labrador Sea and Scotian Shelf, away from the main pole. PC1 shows consistent multidecadal variability with minimums around 1915 and 1980 and maximums around 1940 and 2000. The first mode represents 58.08% of total detrended SSTA variability. Standard deviation between EOFs is largest at the centre of the pole with a maximum of 0.09°C. The highest temporal standard deviation in PC1 is seen at the maximums and minimums previously stated. Even when considering the standard deviation, values for the first mode are significantly different from zero.

Correlation coefficients were determined between the AMO and PC1 over a shared time period, first using the original time series' and then with 10 year running average time series (Table 1). The PC1 uncertainty, calculated using the combined dataset, was used to add randomly generated white noise to the mean PC1, also known as a parametric bootstrap. This process was repeated 100 times allowing us to find a mean and standard deviation of the correlation coefficient. AMO and PC1 have a correlation coefficient of 0.61 ± 0.01. 10-year filtered AMO and PC1 have a correlation coefficient of 0.77 ± 0.02. The first mode shows resemblance to the first mode presented in Loder and Wang (2015), which they also correlated to the AMO. PC1 and NAO have a lower correlation coefficient of 0.03 ± 0.02 for the original time series and -0.01 ± 0.03 for the filtered time series.

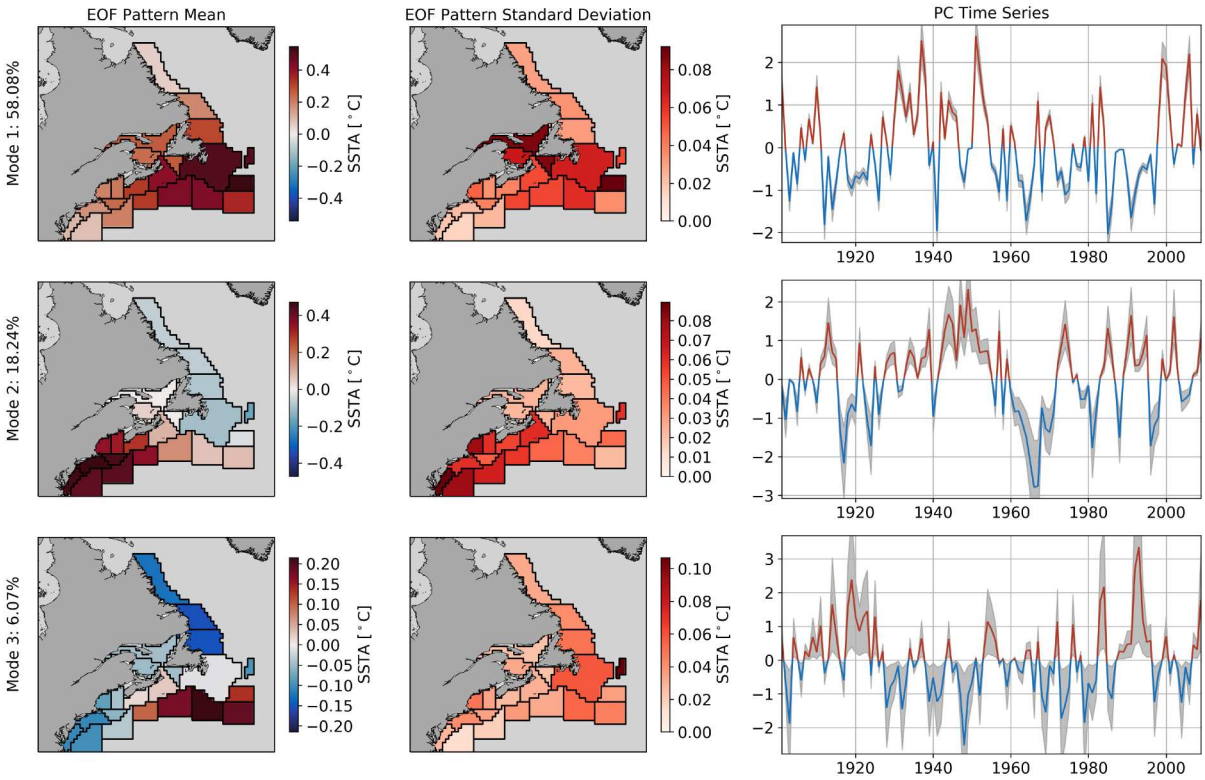

Fig. 3 EOF spatial pattern mean and standard deviation (*first and second columns respectively*) and PC time series (*right column*). The EOFs and PCs correspond to the leading three modes (the rows) from the yearly detrended SSTA EEOF between 1901 and 2010. Positive PC years are shaded in red and negative PC years are shaded in blue, with grey shading showing ±1 standard deviation to represent PC uncertainty in each of the modes. The percentage of explained variability is given in the y axis label of the EOF pattern mean.

TABLE 1. Correlation coefficients at 0 lag between the AMO and NAO index time series from 1901 to 2010 with the original and 10 year running average PC time series. Correlation coefficients were determined for the first three modes.

Original Time Series		
(l)1-3 Mode Number	AMO	NAO
1	0.61 ± 0.01	0.03 ± 0.02
2	0.01 ± 0.03	0.29 ± 0.04
3	−0.16 ± 0.06	0.22 ± 0.06
10 year Running Average Time Series		
Mode Number	AMO	NAO
1	0.77 ± 0.02	−0.01 ± 0.03
2	0.33 ± 0.05	0.41 ± 0.07
3	−0.34 ± 0.11	0.48 ± 0.09

EOF pattern 2 mean (Fig. 3, second row) has a slight negative pole east of Newfoundland and Labrador (regions 10–14) with a minimum of −0.03°C and a positive pole in the Mid-Atlantic Bight (regions 1–6, 14–16) with a maximum of 0.47°C. Maximums in spatial standard deviation are seen around the positive pole but are always less than the magnitude of the pole, therefore implying significance. PC2 again shows dominant multidecadal variability with the highest standard deviations being located at peaks and troughs. Troughs occur around 1915, 1960, and 1980 and peaks occur around 1950 and 2000, the same years where they occur for PC1. The second mode represents 18.24% of total detrended SSTA variability. The highest temporal standard deviation in PC2 is again seen at the maximums and minimums but with larger bounds compared to PC1. Mode 2 looks to have similar multidecadal variability as mode 1, but with additional higher-frequency variability. NAO and PC2 have a correlation coefficient of 0.29 ± 0.04. Filtered NAO and PC2 (through a 10 year running average) have a correlation coefficient of 0.41 ± 0.07. PC2 and AMO have a lower correlation coefficient of 0.01 ± 0.03 for the original time series and 0.33 ± 0.05 for the filtered time series.

EOF pattern 3 mean (Fig. 3, third row) has a positive pole in the eastern slope (regions 17–21) with a maximum of 0.22°C and two negative poles; one located in the Mid-Atlantic Bight (regions 1–4, 14) with a minimum of −0.12°C and one east of Labrador (regions 12–14) with a minimum of −0.15°C. PC3 shows similar multidecadal variability to PC2 and PC1 with maximums and minimums around the same time. The third mode represents 6.07% of the total detrended SSTA variability. The standard deviation in PC3 is consistently as large as the mean PC. Therefore, despite the significance found using the Rule N, I do not consider it a strong signal and so further analysis will not be performed on the third EEOF mode.

b *Heat Flux*

The first two EEOF modes are now compared with regional ocean/atmospheric forcing variables. Positive correlation coefficients between PC1 and $Q_{\mathrm{mdSW}_0} - Q_{\mathrm{mdSW}_{-\mathrm{h}}}$, Q_{LW}, and

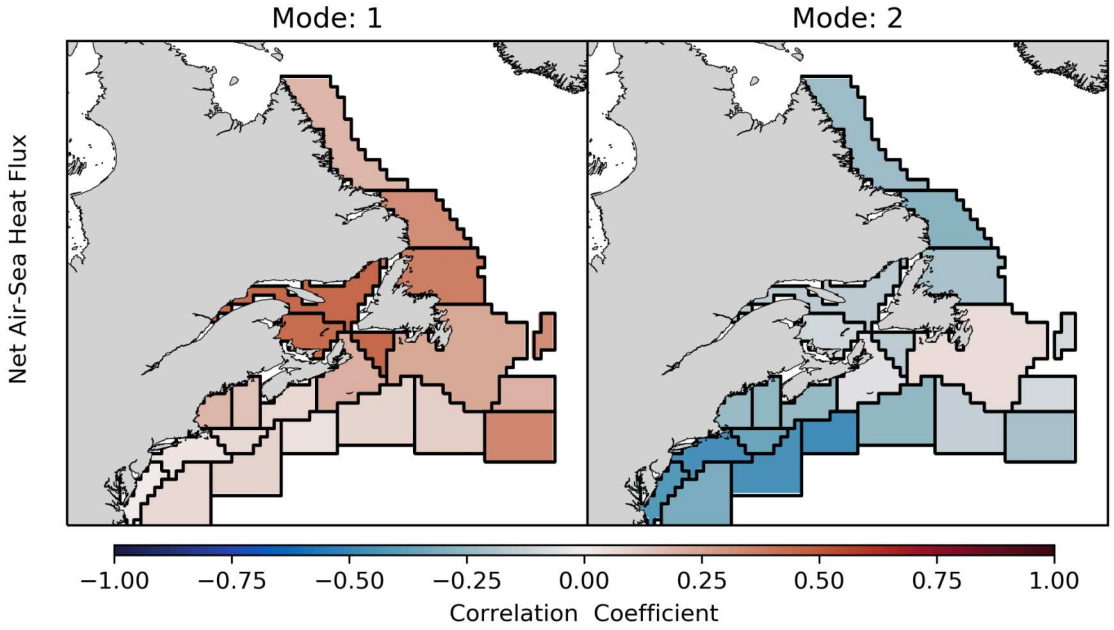

Fig. 4 Correlation coefficient between the mean PC time series for modes 1 (left column) and 2 (right column), with total air-sea heat flux anomaly (Q_{mdSHF}) from 1901 to 2010. Each region of interest is outlined in black and correlation coefficients are constant within each region.

Q_{mdsen} are seen in most areas of interest. Q_{mdlat} and PC1 have a close-to-zero correlation coefficient in most regions (excluding the Gulf of St. Lawrence). Q_{mdSHF} and PC1 have positive correlation coefficients in all areas of interest (Fig. 4).

Negative correlation coefficients are present along the Labrador Coast (regions 12–14) between PC2 and $Q_{\mathrm{mdSW}_0} - Q_{\mathrm{mdSW}_{-h}}$. Positive correlation was found at all other regions. Negative correlation coefficients were found between PC2 and Q_{mdLW}, Q_{mdsen}, Q_{mdlat} and net heat flux in most regions (not shown). Q_{mdSHF} and PC2 have a negative correlation in most regions of interest, including along the Labrador Shelf.

c *Freshwater Flux and Salinity*

Results from the two leading EEOF modes were compared with surface freshwater flux, surface salinity, and depth-averaged salinity. Positive correlation is present for most regions (exluding regions 20, 21) between PC1 and freshwater flux. Negative correlation is present between PC1 and surface salinity from the Northern Scotian Shelf to the Southern Labrador Shelf (regions 7–13; Fig. 5c). Depth-averaged salinity and PC1 have a positive correlation at all regions (excluding regions 8, 12, 13; Fig. 5e).

Freshwater flux and PC2 have a weak negative correlation at all regions excluding from the Gulf of Maine to the Flemish Cap (regions 4–11) where correlation is close-to-zero. Surface salinity and PC2 have a positive correlation from the Mid-Atlantic Bight to the Gulf of Maine, Gulf of St. Lawrence, Northern Newfoundland Coast, and Southern Labrador Shelf (regions 1–5, 8, 9, 12, 13). Negative correlation was found in the Northern Scotian Shelf (region 7) and slope regions 17–20 (Fig. 5d). All other regions are close-to-zero. Depth-averaged salinity and PC2 correlation coefficients have a similar spatial pattern to surface salinity and PC2 (Fig. 5f).

d *Ocean Currents and Wind*

The first two EEOF modes were compared with surface ocean velocity, depth-averaged ocean velocity, and surface wind velocity. PC1 and surface ocean current correlations (Fig. 6a) follow the coastline and are directed northwards. Depth-averaged velocity follows a very similar pattern but with weaker correlation in southern slope and shelf regions (1–5, 15, 19, 20; Fig. 6c). PC1 and surface wind velocity correlations are directed approximately northwest in all regions of interest (Fig. 6e). Along the Labrador Coast, the correlation is directed parallel to the coastline in the northward direction.

PC2 and surface ocean velocity correlations (Fig. 6b) are directed in the southeast direction in northern regions of interest (regions 10–14). In southern regions of interest, the correlation is directed in the northeast direction (regions 1–6, 15, 16). Both correlations collide south of Newfoundland in the slope regions where the correlation is directed east. Depth-averaged velocity and surface wind velocity correlation patterns with PC2 follow a similar spatial pattern to the correlation between surface ocean velocity and PC2.

e *Schematic*

We now present a conceptual model for the formation of an AMO event, and its expression in shelf SSTA (Fig. 7). The formation of a positive AMO event occurs when negative air-sea heat flux anomalies in the Labrador Sea drive Atlantic Meridional Overturning Circulation to advect warm waters north (Wills et al., 2019). This leads to a warming of subpolar

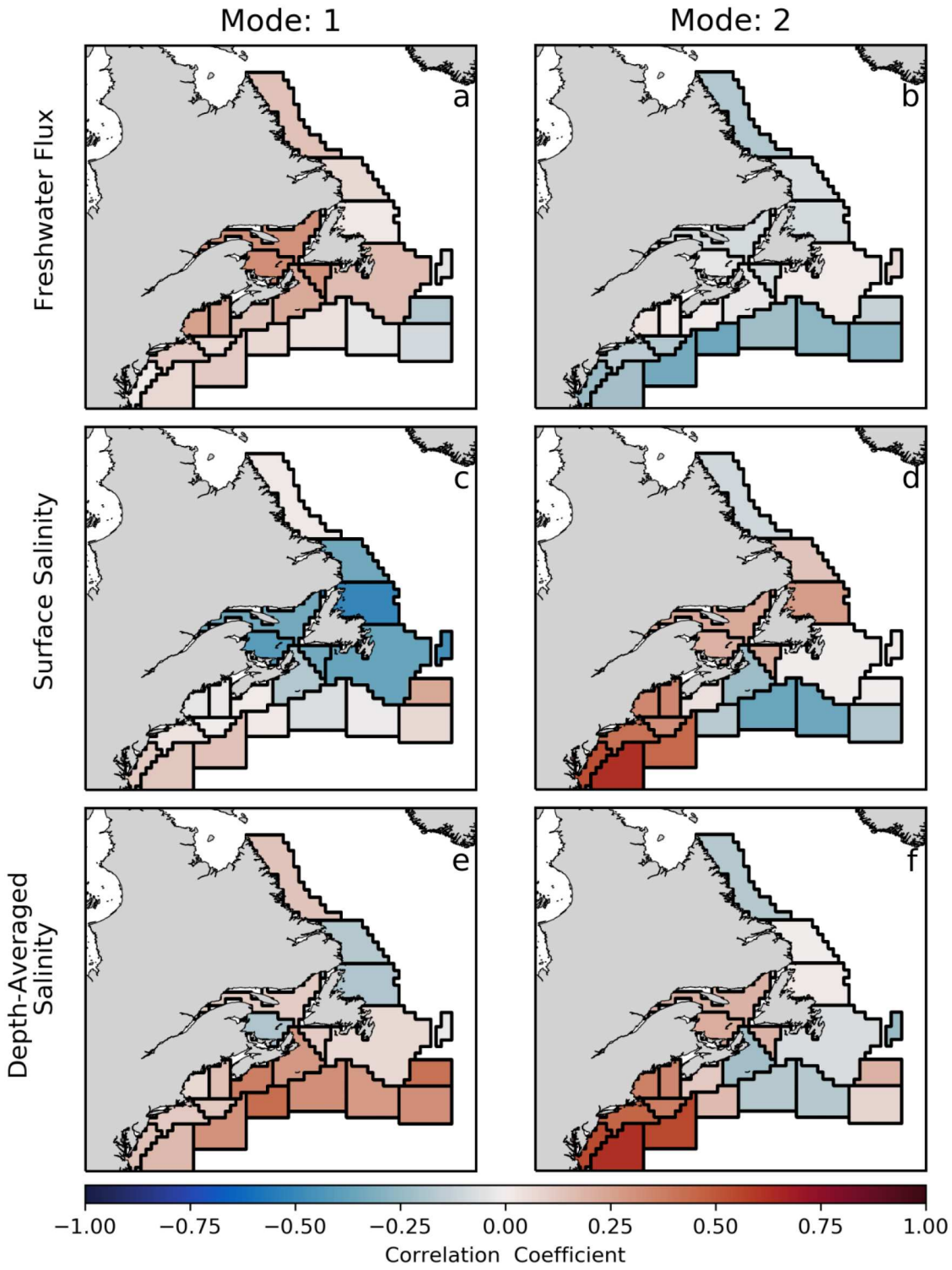

Fig. 5 Correlation coefficient between the mean PC time series 1 and 2, with freshwater flux anomaly, surface salinity anomaly, and depth-averaged salinity anomaly from 1901 to 2010. Each of the variables has also been linearly detrended. Each region of interest is outlined in black and correlation coefficients are constant throughout.

waters after several years. Surface and depth-averaged ocean velocity anomalies correlated with the PC1 highlight this, showing a strengthened Gulf Stream and weakened Labrador Current (Fig. 6, Mode: 1). Consistent positive NAO years create negative heat fluxes in the Labrador Sea (and by extension shelf) driven by strong westerly winds (Wills et al., 2019) (Fig. 7a). This in turn enhances deep water formation and strengthens the Atlantic Meridional Overturning Circulation

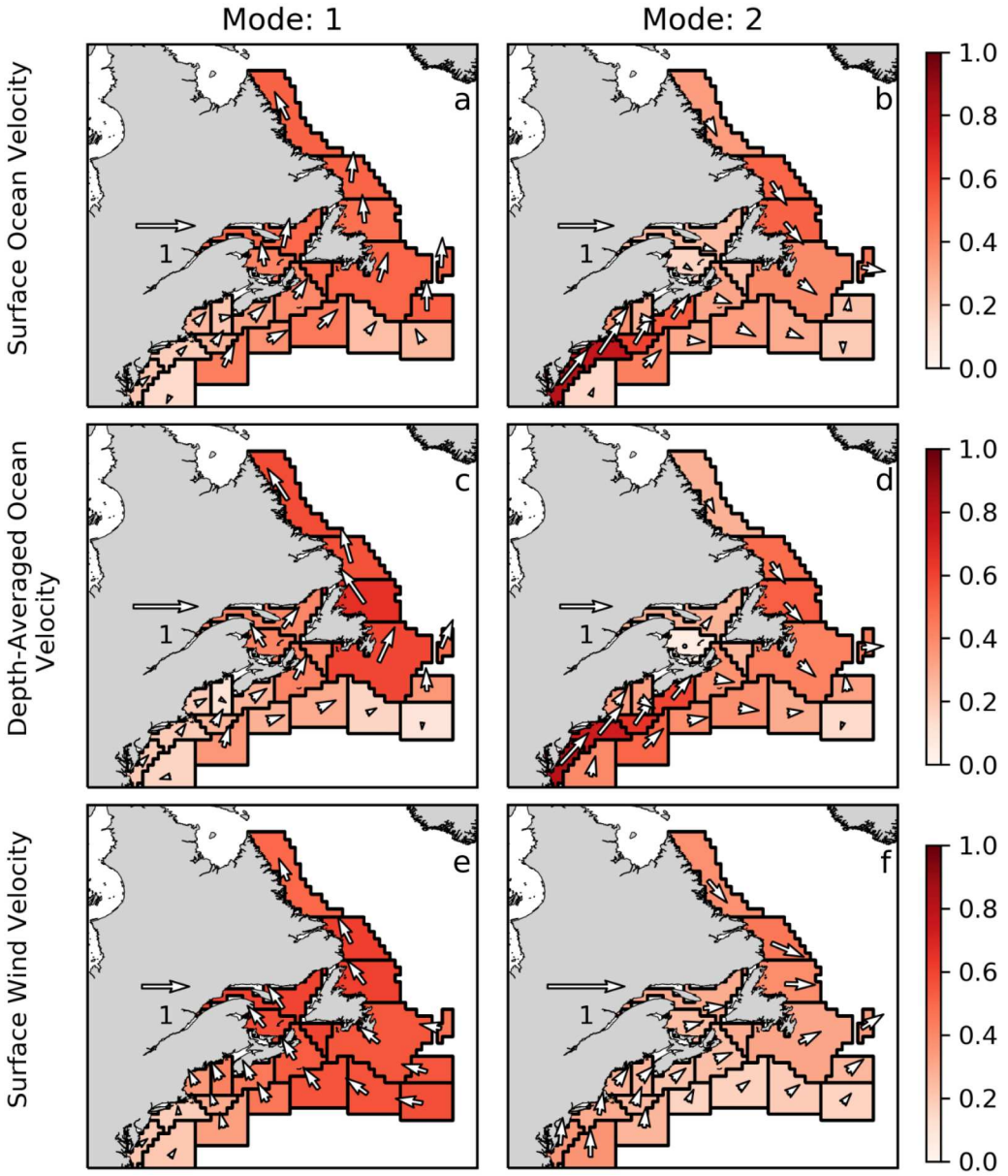

Fig. 6 Correlation coefficient between the mean PC time series 1 and 2, with surface oean velocity anomaly, depth-averaged ocean velocity anomaly, and surface wind velocity anomaly from 1901 to 2010. Each of the variables has also been linearly detrended. Each region of interest is outlined in black and correlation coefficients are constant throughout. The unit correlation arrow is given in each plot. The arrows are defined as (R_u, R_v) where R_u and R_v are the zonal and meridional correlation coefficients for each region.

(Fig. 7b). Therefore consistent positive NAO years could potentially force positive AMO years after several years. Positive NAO years do not have to occur continuously. Positive years as a result of white noise can also cause the formation of positive AMO events (Wills et al., 2019).

Negative air-sea heat flux anomalies and westerly wind velocity anomalies seen in the Labrador Shelf Regions (Figs. 4, 6, Mode: 2) support the positive NAO index hypothesis. After a sufficient time, increased transport of warm water through the Atlantic Meridional Overturning Circulation, causes the formation of a low pressure cell in the Northwest Atlantic subpolar gyre driving warm air northwards. This leads to positive air-sea heat flux anomalies throughout the region (Wills et al., 2019) (Fig. 4, Mode: 1) driven by south easterly winds (Fig. 6, Mode: 1). It is at this point that the positive AMO event reaches a maximum (Fig. 7c).

Total air-sea heat flux anomalies shows a positive correlation with PC1 throughout the Northwest Atlantic coast and shelf regions (Fig. 4, Mode: 1). The increase of air-sea heat flux into the Labrador shelf regions may increase stratification in the region eventually slowing down Atlantic Meridional Overturning Circulation (Deser et al., 2010; Wills et al., 2019). This will lead to a dissipation of the positive AMO event (Fig. 7d).

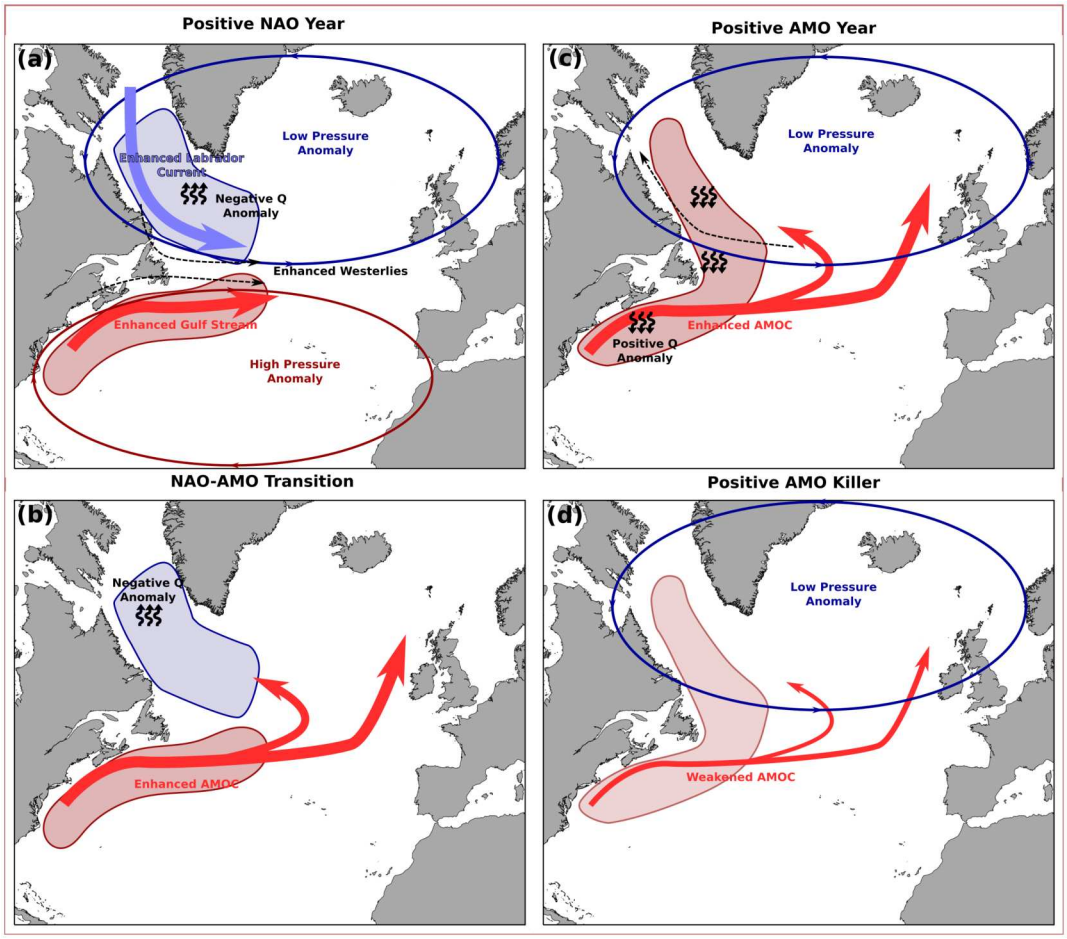

Fig. 7 Schematic of the formation of a positive AMO event. The positive NAO year (a) enhances the Atlantic Meridional Overturning Circulation (AMOC) leading to an NAO-AMO transition (b). After sufficient time, a positive AMO year occurs (c) which is eventually killed by a weakened AMOC (d). Areas of positive (*red shaded area*) and negative (*blue shaded area*) SSTA are shown in each subplot.

The spatial correlation coefficients between PC1 and depth-averaged salinity agree with increased advection of warm salty water through the Gulf Stream (excluding regions 7, 11, 12) (Fig. 5, Mode: 1). Wills et al. (2019) notes increased evaporation over the Labrador Sea region although that is not seen here. Surface salinity shows negative correlation with PC1 throughout most northern regions although this could possibly be due to local precipitation effects.

Correlations between the shelf modes shown here and regional ocean and atmosphere variables support the underlying mechanisms behind the formation of positive AMO index years brought forward by Wills et al. (2019). Restricting for the Northwest Atlantic shelf and slope regions does not noticeably change the governing mechanisms behind variations in PC1 when compared to the whole Northwest Atlantic.

Positive NAO years correspond to a strengthening of the low and high pressure cells centred around Iceland and the Azores respectively. This in turn changes wind velocity magnitude and direction (Deser et al., 2010). Anomalous westerly winds positively correlate to PC2 in regions 8–13 (Fig. 6, Mode: 2). The persistent westerly winds drive the ocean to lose heat (Fig. 3) over the atmosphere resulting in a negative air-sea heat flux (Fig. 4, Mode: 2). This is supported by the negative correlation of Q_{SHF} with PC2.

The mechanism by which the wind changes SST in the region is through Ekman volume and associated heat fluxes. Deser et al. (2010), using similar wind velocities to those found here, showed that the resulting Ekman currents along with latent and surface heat flux drove the di-polar structure seen in EOF2 (Fig. 3). The results of the Ekman currents can be seen in the surface ocean velocity where the typical Labrador Current structure is magnified (Fig. 6, Mode: 2). A similar structure is found in the depth-averaged ocean velocity anomalies (Fig. 6, Mode: 2) but it is unclear whether this is driven exclusively by the anomalous Ekman current. Increased cold water transport in the Labrador Shelf regions driven by Ekman currents results in negative SSTA from the Grand Banks up to the Labrador Shelf (regions 9–13) (Fig. 3). A similar opposite result occurs with the magnified Gulf Stream, resulting in anomalously warm waters in the southern shelf and slope (regions 1–7, 15–20) (Fig. 3).

Diminished wind velocity anomalies correlated to PC2 (Fig. 6) in the southern shelf and slope (regions 1–8, 15–21) show less

prominent westerlies therefore losing less heat to the atmosphere. Deser et al. (2010) notes anomalous easterly surface wind velocities at the mid-latitudes. The restraints in the spatial domain or spatial averaging could explain the lack of easterlies seen here.

With increased advection through the Labrador Current and Gulf Stream, we would expect to see negative surface salinity anomalies along the Labrador Shelf and positive surface salinity anomalies in the south. Mid-shelf, slope, and Labrador shelf regions do not support this hypothesis. It is possible that despite increased advection of warm salty water from the south and cold fresh water from the north, other processes result in the shown surface salinity anomalies.

4 CESM2 heat budget results

We now turn to climate modelling to better understand the relevant heat budget processes at play in the variability identified in Section 3 as well as the role of the AMO and NAO.

a *CESM2-defined AMO and NAO*

Yearly-averaged AMO and NAO indices were created for each of the ten CESM2-LENS ensemble members (Fig. 8). The time series includes the ensemble mean, ±1 ensemble standard deviation, and the annual observed AMO and NAO indices. The CESM2-derived AMO index (Fig. 8, top plot) mean and standard deviation show a clear multidecadal oscillation with positive phases approximately located at 1875–1900, 1920–1950, and 1990–2015. The observed AMO index also shows positive phases at approximately the same time (Trenberth & Shea, 2006). The individual ensemble member AMO indices are not always temporally consistent with individual peaks being seen around 1960–1970 and 1970–1985. Negative phases are also consistent between the CESM2-derived and observed AMO indices. Troughs can be seen in both around 1900–1920 and 1960–1990. The spread (standard deviation) of the CESM2-derived AMO indices is temporally consistent staying around ± 0.5°C for the entire time series.

The individual ensemble CESM2-derived NAO indices (Fig. 8, bottom plot) show a much higher frequency of variability when compared to the ensemble mean AMO index. This is again mirrored in the observed NAO index (Hurrell et al., 2003). The mean of the CESM2-derived NAO index has a lower amplitude than each of the individual ensemble NAO indices. This suggests that the NAO indices are out of phase across ensemble members. This is the opposite to the individual ensemble members AMO indices where the phases mostly line up. The observed NAO index also shows a yearly-to-multiyear oscillation similar to the NAO indices derived from the CESM2-LENS. Upon first observation, it is difficult to determine similarities between the in-situ and CESM2-derived NAO indices due to the increased frequency of oscillation.

High correlation coefficients were found between the mean CESM2-derived AMO index and the observed AMO index (0.45 at lag 0). There is also a clear wave pattern to the cross-correlation with peaks around −65 years and 65 years lag (not shown). This suggests a multidecadal structure in both the CESM2-derived and observed AMO indices, one that can be clearly seen in both of the time series (Fig. 8, top plot). Most AMO indices of the individual ensemble members follow the mean. However, there are noticeable differences around the 65 year lag peak. Consistently low

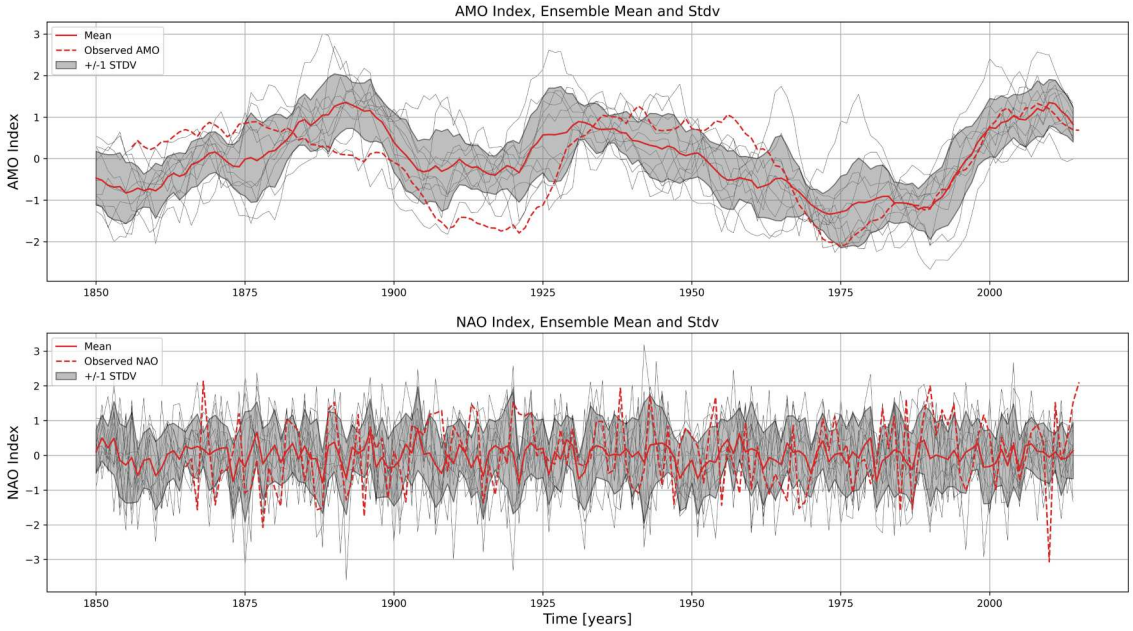

Fig. 8 Annual CESM2-derived AMO (*top plot*) and NAO (*bottom plot*) indices from 1850 to 2015. The individual ensemble member (*solid grey lines*), the mean index (*solid red line*) and ±1 ensemble standard deviation (*grey shaded area*) are shown for both the AMO and NAO indices. The observed AMO and NAO indices (*dashed red line*) are also shown.

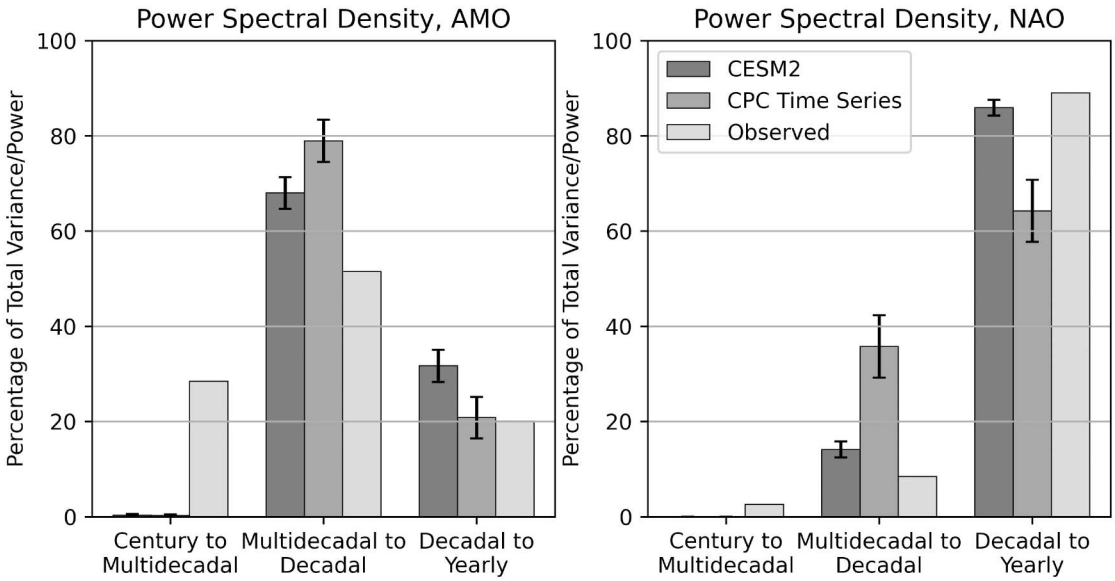

Fig. 9 Power spectral density plots for the observed, CESM2-derived, and CPC time series AMO (*left column*) and NAO (*right column*) indices. The power spectral density plots were integrated over three defined periods; century to multidecadal, multidecadal to decadal, and decadal to yearly. The mean and standard deviation of the CESM2-derived AMO and NAO indices and CPC time series (*left and middle bars, darker colouring*) is shown along with the power spectral density plot for the observed AMO and NAO index (*right bars, lighter colouring*).

correlation coefficients were found between the CESM2-derived and observed NAO indices (−0.005 at 0 years lag). The mean correlation coefficient is also lower than the individual ensemble members indices suggesting that they are out of phase similar to what occured in the CESM2-derived NAO time series (Fig. 8, bottom plot).

The power spectral densities for AMO and NAO indices were integrated over specific frequencies and divided by the total power spectral density sum to determine the percentage of total variance/power that is found in century to multidecadal (100+ to 100 year period), multidecadal to decadal (100 to 10 year period), and decadal to yearly periods (10 to 1 year period) (Fig. 9). Most (68.37% $\pm$ 3.32%) of the CESM2-derived AMO indices total variance is found in periods larger than 10 years (Fig. 9, left plot). This is again the result of the strong multidecadal signal seen in the AMO time series (Fig. 8, top plot). The vast majority (82.25%) of the observed AMO index variance is within the century to multidecadal and multidecadal to decadal periods. This is expected as both the CESM2-derived and observed AMO indices oscillate with a period of 60–80 years (Deser et al., 2010; Trenberth & Shea, 2006). The decadal to yearly percentage of total variance for both CESM2-derived and in-situ AMO indices is relatively low, 31.19% $\pm$ 3.42% for the CESM2-derived AMO indices and 17.75% for the observed AMO index.

For the CESM2-derived NAO indices, 14.15% $\pm$ 2.08% of the variance is found within the multidecadal to decadal period rage and 85.85% $\pm$ 2.08% is found within the decadal to yearly period range (Fig. 9, right plot). For the in-situ NAO index, 18.54% is found within the century to multidecadal and multidecadal to decadal period range and 81.46% is found within the decadal to yearly period range. This suggests that although the phasing between the ensemble members NAO indices with the in-situ NAO index is off, both groups contain similar time scales of variability.

b *Modes of Variability in CESM2-LENS*

An EOF was performed on the detrended mixed layer temperature tendency anomaly from each of the ten ensemble members between 1850 and 2015. Using the ensemble member's resulting EOF eigenvalues, it was found that modes one and two explained 57.0 $\pm$ 3.0% and 20.0 $\pm$ 3.0% respectively; collectively explaining 77% $\pm$ 6.0%.

EOF mean spatial pattern 1 (Fig. 10, first row) has a positive sign throughout most of the regions with a positive pole locate east of Newfoundland. The mode decays to the north and south, over the Labrador Sea and Mid-Atlantic Bight, away from the main pole. The standard deviation across EOFs from all ensemble members increases towards the Mid-Atlantic Bight where the mean EOF is smallest. The mean values in the pole structure are always higher than the corresponding standard deviation. The first modes spatial pattern shows resemblance to the first modes correlated with the AMO from Loder and Wang (2015, 2024).

CPC1 shows a consistent multidecadal variability with positive phases peaking around 1930 and 2005 and a negative phase around 1980. The CESM2-derived AMO index mostly mirrors CPC1 after 1910 and before 1875. Between these years, the AMO index shows a clear increase around 1900 which is not mirrored in the CPC1 time series. The first mode explains 57.0 $\pm$ 3.0% of the total detrended mixed layer temperature tendency anomaly variance. The CPC1

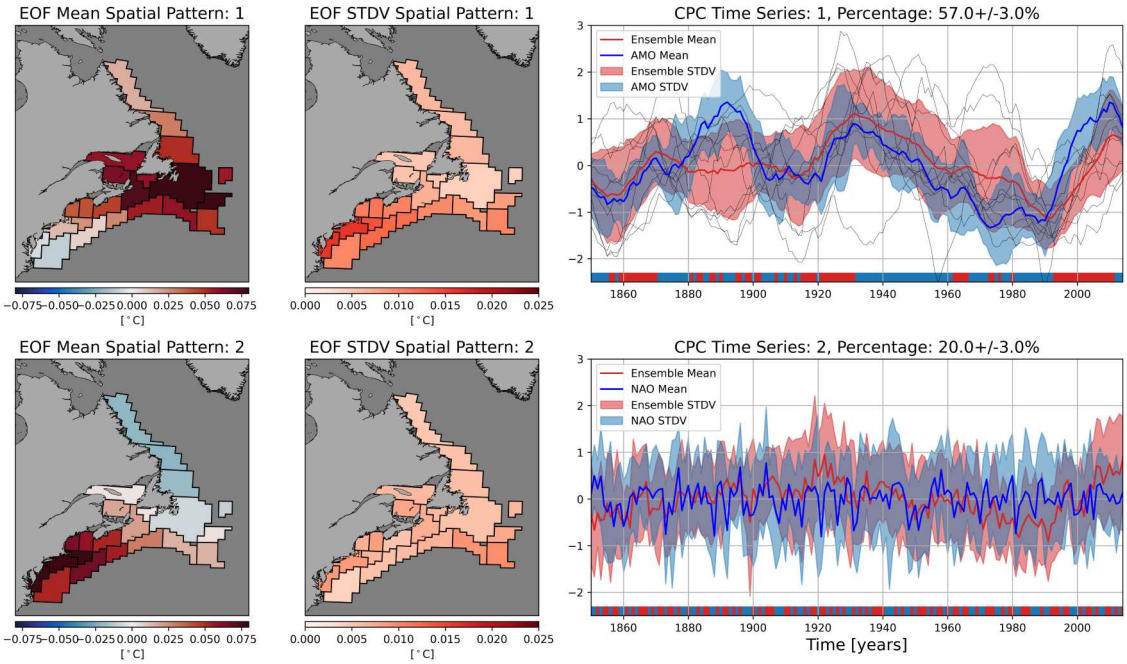

Fig. 10 EOF spatial pattern mean and standard deviation (*first and second columns respectively*) and CPC time series (*right column*). The EOF and CPC rows correspond to the leading two modes from the yearly detrended mixed layer temperature tendency anomaly between 1850 and 2015. The CPC time series mean (*solid red line*) and standard deviation (*shaded red area*) along with the CESM2-derived AMO and NAO mean (*solid blue line*) and standard deviation (*shaded blue area*) are shown (*right column*). The percentage of explained variability is given above the CPC time series. The first mode also includes each of the individual ensemble members PC time series (*grey lines*). Positive gradient formation years (*red areas*) for the mean CPC1 and CPC2 are shown along the bottom of the time series. Negative dissipation years are also shown (*blue areas*).

ensemble spread (standard deviation about the mean) has a similar magnitude of ±0.75 until the beginning of the 1980s when the standard deviation decreases. The CESM2-derived AMO ensemble spread is consistently less than the spread for the CPC1, at around ±0.5 for the entire time series.

EOF mean spatial pattern 2 (Fig. 10, second row) has a dipolar structure with a positive pole in the Mid-Atlantic Bight and a slight negative pole in the Labrador Sea. The standard deviation of the spatial pattern shows consistently lower values than the mean throughout all regions. This is similar to the second mode correlated with the NAO from Loder and Wang (2015, 2024).

CPC2 shows higher frequency variability throughout the time series superimposed onto a multidecadal oscillation. A clear multidecadal peak can be seen around 1920–1930 and 2000–2015 and a trough around 1850–1860 and 1970–1980. The CESM2-derived NAO index also shows high frequency variability but does not exhibit a multidecadal signal like in the CPC2. The second mode explains 20.0 $\pm$ 3.0% of the total detrended mixed layer temperature tendency anomaly variance. Both the CESM2-derived NAO indices and CPC2 have a much higher spread (standard deviation) than the reported mean indicating that the ensemble members time series are out of phase with one another.

The CESM2-derived AMO and NAO indices were cross-correlated with the two leading PC time series from the EOF results. The CPC1 and CPC2 time series were compared with the CESM2 ensemble mean AMO or NAO index. Peak correlation values are 0.29 for CPC1/AMO and 0.18 for CPC2/NAO, both at lag 0 (not shown).

The first CPC time series' power spectral density, indicates that 79.12% $\pm$ 4.35% of the variance is within the multidecadal to decadal period window and 20.80% $\pm$ 4.35% is within the decadal to yearly period window (Fig. 9, left plot). This is similar to the power spectral densities of the CESM2-derived and observed AMO indices and establishes that all three index groups feature prominent multidecadal oscillation. The second CPC time series' power spectral density indicates that 35.76% $\pm$ 6.53% of the variance is within the multidecadal to decadal period window and 64.24% $\pm$ 6.53% is within the decadal to yearly period window (Fig. 9, right plot). Therefore, both the CPC-derived NAO and CESM2-derived NAO have a similar power spectral density to the observed NAO index.

Results from the cross-correlations, power spectral density plots, and EOF indicate that both the CESM2-derived AMO and NAO indices and CPC time series appear to be representations of the observed AMO and NAO indices and their associated SSTA spatial patterns (Deser et al., 2010; Hurrell et al., 2003; Loder & Wang, 2015, 2024; Trenberth & Shea, 2006). We assume that because of the representation of the observed AMO and NAO in the CESM2-LENS temperature tendency output, that the physical forcing behind these model-generated AMO and NAO indices is also representative.

c *Anomaly Heat Budget*

A temperature tendency anomaly heat budget was created for each of the regions from 1850 to 2015. Years were defined as positive (formation) or negative (dissipation) according to the value of the PC times series in Section b. The average over all positive years or negative years (composite mean) of each of the heat budget terms across all ensemble members was then calculated and removed from the original terms to leave anomalies; we refer to this as "anomaly heat budget". The standard deviation across ensemble members was also calculated.

1 FIRST MODE HEAT BUDGET

The composite mean temperature tendency for positive PC1 (Fig. 11, light grey bar) follows a similar pattern to the results from the EOF first spatial pattern. Temperature tendency increases towards the location of the positive pole east of Newfoundland (region 10). This increase in temperature tendency is seen in both the shelf regions (7, 8, 9, 10, 11, 12) and slope regions (18,19,20,21). The standard deviation of the temperature tendency across ensemble members in these regions remains relatively small compared to the mean. The mean AMO formation temperature tendency

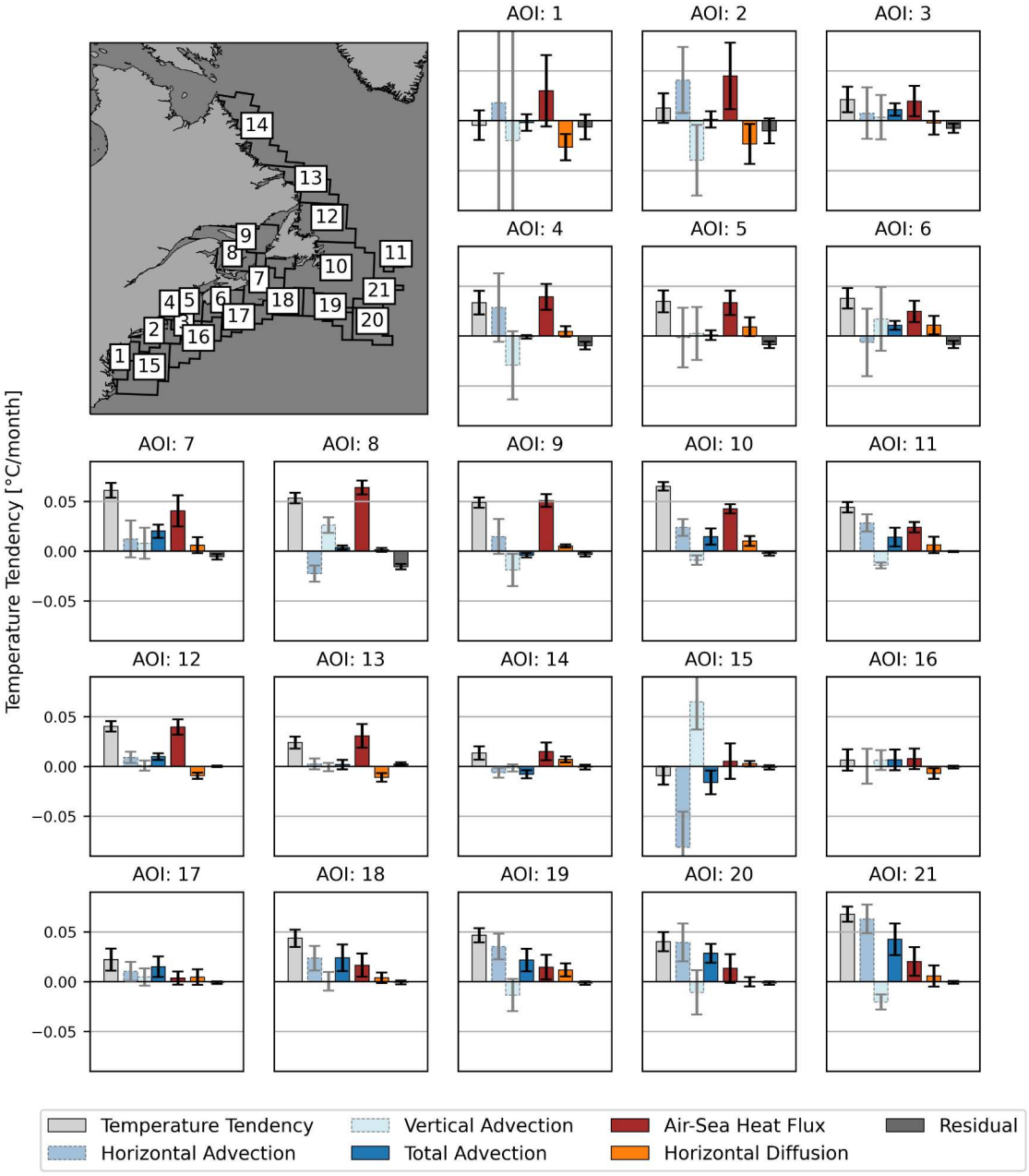

Fig. 11 Region of interest heat budget terms [°C/month] averaged over positive PC time series 1 years. Each term has a ±1 standard deviation uncertainty bar calculated from the ensemble means standard deviation. The horizontal and vertical components of the total advection term (*dark blue*) are shown to left (*dotted outlines, lighter colouring*). The sum of all darker coloured bars equals the temperature tendency (*light grey*) plus the residual (*dark grey*). A reference map is given in the top left corner with each of the regions labelled.

accurately recreate the AMO SSTA spatial pattern (Fig. 10, first row). Throughout most of the regions, the residual temperature tendency (dark grey bar) remains small relative to most of the other heat budget terms.

The total advection (Fig. 11, dark blue bar) varies in its contribution to the total temperature tendency depending on region. In the shelf regions (1–14), the total temperature tendency mostly plays a minimal role in the positive total temperature tendency. This is especially the case in regions 1–6, 8, and 9. In some regions, the horizontal advection temperature tendency is equal and opposite to the vertical advection temperature tendency (region 1, 2, 15). This implies a compensation such that heat advected into the region, either horizontally or vertically, is immediately advected out in the other direction. In regions 7, 10, and 11, the total advection temperature tendency helps to contribute to the positive total temperature tendency but is not the main contributor to the positive mean. In contrast, the slope regions (15–21) total temperature advection is mostly the main contributor to positive total temperature tendency where a strong positive signal can be found (region 17–21).

The air-sea heat flux (Fig. 11, dark red bar) also varies depending on whether the region is located on the slope or shelf. In most of the shelf regions with positive total temperature tendencies, the air-sea heat flux is the main contributor to the positive signal. This is apparent in regions 7–10. In the slope regions that show a strong positive signal (region 17–21), the air-sea heat flux contributes roughly the same or less than the positive signal seen in the total advection.

Outside of regions 1 and 2, the horizontal diffusion temperature tendency accounts for a minimal amount of the positive temperature tendency anomaly signal. Within regions 1 and 2, the horizontal diffusion term also has a large standard deviation.

2 FIRST MODE COMPOSITE MEANS

Ensemble means of candidate forcing variables were averaged over the first mode's positive years (Figs. S1, S2). Variables were selected that either directly or indirectly appear in the heat budget equation. For each variable, anomalies were determined and then detrended. All variables, except mixed layer ocean velocity anomaly and surface wind stress anomaly, were spatially averaged into the regions of interest. Regions with air-sea heat flux component standard deviations larger than the mean are represented with a dashed region outline.

During positive PC1 years, the mixed layer ocean velocity anomaly along the slope is not spatially consistent. Two large anomalous gyres can be seen in the slope regions off the Mid-Atlantic Bight (region 15, 16) and to the southeast of Newfoundland (region 10, 19–21). The magnitude of the mixed layer ocean velocity anomaly in the northeast direction in the southern slope and shelf is the result of these two gyres. Regions 17 and 18 between the two anomalous gyres has a relatively smaller anomaly. The two furthest east slope regions (20, 21) show the mixed layer ocean velocity anomaly travelling in the opposite direction to most of the regions located on the slope. The southern shelf regions (1–11) show no clear structure. The northern shelf regions (12–14) show a slight increase in northward flow. This is all consistent with a reduction in the Labrador Current over our whole region.

The surface wind stress anomaly shows a clear structure throughout all regions. In the southeast, the surface wind stress anomaly is directed west. In the northwest, it is directed north. This implies a larger clockwise rotation and is linked to an atmospheric high pressure cell located in the Labrador Sea.

The total air-sea heat flux, sensible heat flux, and latent heat flux of vaporization all show a similar significant positive polar structure to what is seen in the total temperature tendency (Fig. S2). Along the shelf, sensible heat flux and latent heat flux of vaporization both contribute roughly the same amount to the total positive signal (regions 4–9). In the Grand Banks and Flemish Cap, latent heat flux of vaporization has a higher positive anomaly than sensible heat flux (regions 10, 11). In the eastern slope regions, latent heat flux of vaporization consistently shows higher postive anomalies when compared to sensible heat flux (regions 17–21). Shortwave heat flux anomalies are insignificant outside of the western slope regions (15–18) and the northern Gulf of St. Lawrence (region 9).

3 SECOND MODE HEAT BUDGET

The same averaging over positive years of heat budget terms was done for the second mode PC time series (Fig. 12). For the second mode, positive and negative years correspond to NAO formation and dissipation years respectively.

The composite mean heat budget for positive PC2 years (Fig. 12) is consistent with the spatial pattern seen in the second mode EOF spatial pattern (Fig. 10, second row). The positive pole is located around the Mid-Atlantic Bight (regions 1–3) and a weaker negative pole is located along the Labrador Shelf (regions 12–14). The temperature tendency anomaly during NAO formation years recreate the NAO SSTA spatial pattern (Fig. 10). In both poles, the main contributor to the temperature tendency is the air-sea heat flux.

The total advection in both the positive and negative poles is relatively small for most regions. In many of the regions the horizontal advection balances out the vertical advection term (regions 1–6, 15, 16). Horizontal diffusion also contributes very little to the temperature tendency term in both the poles.

Air-sea heat flux is the main contributor to the dipolar structure in both the shelf and slope regions. The residual is low across all regions except 1 and 2 but still remains lower than the relative temperature tendency and air-sea heat flux terms.

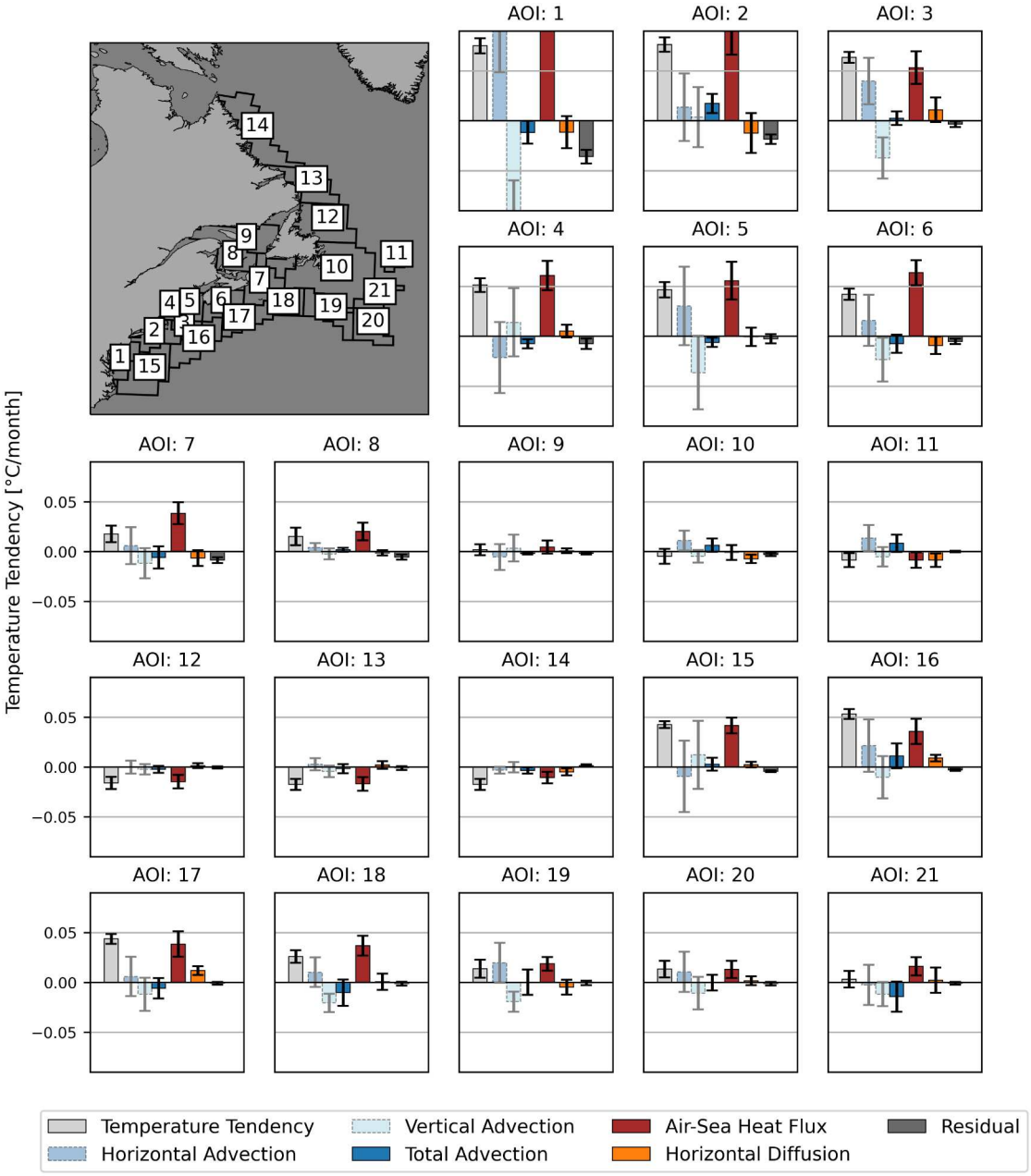

Fig. 12 Region of interest heat budget terms [°C/month] averaged over positive PC2 years. Each term has a ±1 standard deviation uncertainty bar calculated from the ensemble means standard deviation. The horizontal and vertical components of the total advection term (*dark blue*) are shown to left (*dotted outlines, lighter colouring*). The sum of all darker coloured bars equals the temperature tendency (*light grey*) plus the residual (*dark grey*). A reference map is given in the top left corner with each of the regions labelled.

4 COMPOSITE MEANS SECOND MODE

The mixed layer ocean velocity anomalies during positive PC2 time series years show an overall weakening of the Gulf Stream and Labrador Current (Fig. S3). The weakening of the Gulf Stream mainly occurs along the slope regions except for in region 2 where the anomalous mixed layer ocean velocity goes in the opposite direction. In many of the shelf regions, the mixed layer ocean velocity anomaly is close to zero, especially in the regions located in the middle of the previously mentioned dipolar structure (regions 7–11).

The surface wind stress anomalies during positive years shows an overall clockwise flow from which we can associate a high pressure cell (Fig. S3). The regions located in the middle of the dipolar structure (regions 7–11, 19–21) have a close to zero surface wind stress anomaly.

The total air-sea heat flux, longwave heat flux, sensible heat flux, and latent heat flux of vaporization all have an anomalous dipolar structure with a negative pole in the southern regions and a lesser positive pole in the northern regions (Fig. S4). The shortwave and latent heat flux of fusion were found be insignificant for most regions. The

northern pole is mainly made up of the longwave heat flux and sensible heat flux anomalies. The southern pole can be mainly attributed to sensible heat flux and latent heat flux of vaporization anomalies.

5 Conclusion

Here we have documented the yearly-to-multidecadal variability in SSTA along the Northwest Atlantic shelf and slope, including physical processes and uncertainty. Throughout this paper, an emphasis was put on determining uncertainty in calculations through the use of multiple data products and ensemble members. Five different global SST data products were used and the subsequent analysis considered them all jointly, as representing spread about an unknown true SST. An EEOF was used, allowing all data products to be considered together, rather than the standard EOF, in order to consider cross-data product variability when defining Northwest Atlantic modes of variability. The novel use of the CESM2-LENS output allowed for the creation of a heat budget over a 165-year time period covering the entire Northwest Atlantic shelf and slope from the Mid-Atlantic Bight to the Labrador Shelf.

Significant modes of SSTA variability along the Northwest Atlantic shelf and slope were isolated and linked to the AMO and NAO climate modes. By comparing the resulting AMO and NAO indices with ocean/atmospheric variables known to have an effect on SST, further evidence was found to support how positive NAO years lead to the eventual formation of a positive AMO event (Wills et al., 2019). Surface mixed layer heat budget results show that the formation and dissipation of positive AMO years is driven by air-sea heat flux anomalies in slope regions and by a combination of horizontal advection and air-sea heat flux anomalies in shelf regions. The resulting heat budget terms provided further evidence that positive NAO years increase warm water flow northwards eventually preceeding the formation of positive AMO years (Wills et al., 2019). Heat budget results also showed that the formation and dissipation of positive NAO years is mainly driven by anomalous air-sea heat flux. This matches the current understanding of the NAO physical forcing (Deser et al., 2010).

In this paper we did not consider anthropogenic climate change. How would the heat budget change if we were to include the projected future (2015–2100) portion of the climate model output? Do long-term ocean temperature trends affect the AMO and NAO spatio-temporal SSTA patterns (and by extension mixed layer temperature tendency anomaly patterns)? How is anthropogenic climate change expressed as a local physical ocean process? These are important questions as they help us to determine the possible strength and predictability of future SSTA variability in the Northwest Atlantic.

The novel use of multiple ensemble members when determining our heat budget results allowed for the calculation of uncertainty values for all results. When using climate model output, it is recommended that all ensemble members be used so that ensemble variability is included in future results. When possible, an emphasis should be put on considering cross-dataset variability and determining the corresponding uncertainty in any trend and variability calculations. An example of this is the use of an EEOF, which allows for multiple EOF spatial patterns or PC time series.

There are limitations to how we have considered uncertainty. First, observation-based data products in this paper were used blindly, with each data product considered as one realization of the true unknown SST. Uncertainty in the individual data products was not considered when calculating the mean and standard deviation of the SST ensemble. In the future, an assessment of uncertainty could be conducted for each of the data products. Second, climate model output was used for heat budget results rather than observation-based data products. It is important to note that models do not perfectly recreate observations, and so will provide a source of uncertainty when interpretting the physical dynamics. Lastly, EOF results were used to isolate AMO and NAO positive and negative years rather than the CESM2-derived AMO and NAO. This allows for differences between the PC time series and AMO and NAO to carry over into the heat budget and composite mean results.

The importance of understanding the physical forcing behind multidecadal oscillation in the Northwest Atlantic has become more important than ever with increasing ocean temperatures. In this paper, an initial understanding of how the SSTA spatio-temporal patterns associated with the AMO and NAO climate modes occurs along the Northwest Atlantic shelf and slope is presented. Further research is recommended on how to accurately predict future Northwest Atlantic shelf and slope multidecadal variability as its impact on regional climate, local communities, and marine ecosystems cannot be ignored.

Disclosure statement

No potential conflict of interest was reported by the author(s).

Funding

This work was supported by a National Sciences and Engineering Research Council (NSERC) Discovery Grant (RGPIN-2018-05255, "Prediction and predictability of climate extremes") and a NSERC Strategic Partnership Grants for Projects ("Climate and Ocean Dynamics Informing Resource Management and Adaptation Policy (CODREMAP)").

ORCID

J. Coyne http://orcid.org/0009-0008-5181-9055
E. Oliver http://orcid.org/0000-0002-4006-2826

Supplemental data

Supplemental data for this article can be accessed at https://doi.org/10.1080/07055900.2025.2530439.

References

Chen, K., Ruoying, H., Powell, B. S., Gawarkiewicz, G. G., Moore, A. M., & Arango, H. (2014). Data assimilative modeling investigation of Gulf Stream Warm Core Ring interaction with continental shelf and slope circulation. *Journal of Geophysical Research: Oceans*, *119*(9), 5968–5991. https://doi.org/10.1002/jgrc.v119.9

Chen, S., Chen, W., Zhou, W., Wu, R., Ding, S., Chen, L., He, Z., & Yang, R. (2024). Interdecadal variation in the impact of Arctic Sea Ice on the El Niño-Southern oscillation: The role of atmospheric mean flow. *Journal of Climate*, *37*(21), 5483–5506. https://doi.org/10.1175/JCLI-D-23-0733.1

Chen, S., Wu, R., & Chen, W. (2020a). Strengthened connection between springtime North Atlantic oscillation and North Atlantic tripole SST pattern since the late 1980s. *Journal of Climate*, *33*(5), 2007–2022. https://doi.org/10.1175/JCLI-D-19-0628.1

Chen, S., Wu, R., & Chen, W. (2020b). Structure and dynamics of a springtime atmospheric wave train over the North Atlantic and Eurasia. *Climate Dynamics*, *54*(11–12), 5111–5126. https://doi.org/10.1007/s00382-020-05274-7

Chen, S., Wu, R., Chen, W., Hu, K., & Yu, B. (2021). Influence of North Atlantic sea surface temperature anomalies on springtime surface air temperature variation over Eurasia in CMIP5 models. *Climate Dynamics*, *57*(9–10), 2669–2686. https://doi.org/10.1007/s00382-021-05826-5

Chen, Z., Kwon, Y. O., Chen, K., Fratantoni, P., Gawarkiewicz, G., & Joyce, T. M. (2020). Long-term SST variability on the Northwest Atlantic continental shelf and slope. *Geophysical Research Letters*, *47*(1), 1–11.

Deser, C., Alexander, M. A., Xie, S. P., & Phillips, A. S. (2010). Sea surface temperature variability: Patterns and mechanisms. *Annual Review of Marine Science*, *2*(1), 115–143. https://doi.org/10.1146/marine.2010.2.issue-1

Enfield, D. B., Mestas-Nunez, A. M., & Trimble, P. J. (2001). The Atlantic multidecadal oscillation and its relation to rainfall and river flows in the continental U.S. *Geophysical Research Letters*, *28*(10), 2077–2080. https://doi.org/10.1029/2000GL012745

Giese, B. S., Seidel, H. F., Compo, G. P., & Sardeshmukh, P. D. (2016). An ensemble of ocean reanalyses for 1815–2013 with sparse observational input. *Journal of Geophysical Research: Oceans*, *121*(9), 6891–6910. https://doi.org/10.1002/jgrc.v121.9

Han, G. (2003). Three-dimensional seasonal-mean circulation and hydrography on the eastern Scotian Shelf. *Journal of Geophysical Research*, *108*(C5), 1–21. https://doi.org/10.1029/2002JC001463

Han, G., Chen, N., & Ma, Z. (2014). Is there a north-south phase shift in the surface Labrador Current transport on the interannual-to-decadal scale? *Journal of Geophysical Research: Oceans*, *119*(1), 276–287. https://doi.org/10.1002/jgrc.v119.1

Hilmer, M., & Jung, T. (2000). Evidence for a recent change in the link between the North Atlantic Oscillation and Arctic sea ice export. *Geophysical Research Letters*, *27*(7), 989–992. https://doi.org/10.1029/1999GL010944

Hirahara, S., Ishii, M., & Fukuda, Y. (2014). Centennial-scale sea surface temperature analysis and its uncertainty. *Journal of Climate*, *27*(1), 57–75. https://doi.org/10.1175/JCLI-D-12-00837.1

Holbrook, N. J., Scannell, H. A., Sen Gupta, A., Benthuysen, J. A., Feng, M., E. C. J. Oliver, Alexander, L. V., Burrows, M. T., Donat, M. G., Hobday, A. J., Moore, P. J., Perkins-Kirkpatrick, S. E., Smale, D. A., Straub, S. C., & Wernberg, T. (2019). A global assessment of marine heatwaves and their drivers. *Nature Communications*, *10*(1), 1–13. https://doi.org/10.1038/s41467-019-10206-z

Huang, B., Thorne, P. W., Banzon, V. F., Boyer, T., Chepurin, G., Lawrimore, J. H., Menne, M. J., Smith, T. M., Vose, R. S., & Zhang, H.-M. (2017). Extended reconstructed sea surface temperature, Version 5 (ERSSTv5): Upgrades, validations, and intercomparisons. *Journal of Climate*, *30*(20), 8179–8205. https://doi.org/10.1175/JCLI-D-16-0836.1

Hurrell, J. W., Kushnir, Y., Ottersen, G., & Visbeck, M. (2003). An overview of the North Atlantic oscillation. *Geophysical Monograph Series* 134, 1–35. American Geophysical Union (AGU).

Kent, M., Kent, E. C., & Kennedy, J. J. (2021). Historical estimates of surface marine temperatures. *Annual Review of Marine Science*, *13*(1), 283–311. https://doi.org/10.1146/marine.2021.13.issue-1

Laloyaux, P., de Boisseson, E., Balmaseda, M., Bidlot, J.-R., Broennimann, S., Buizza, R., Dalhgren, P., Dee, D., Haimberger, L., Hersbach, H., Kosaka, Y., Martin, M., Poli, P., Rayner, N., Rustemeier, E., & Schepers, D. (2018). CERA-20C: A coupled reanalysis of the twentieth century. *Journal of Advances in Modeling Earth Systems*, *10*(5), 1172–1195. https://doi.org/10.1029/2018MS001273

Large, W. G., Danabasoglu, G., Doney, S. C., & Mcwilliams, J. C. (1997). Sensitivity to surface forcing and boundary layer mixing in a global ocean model: Annual-mean climatology. *Journal of Physical Oceanography*, *27*(11), 2418–2447. https://doi.org/10.1175/1520-0485(1997)027¡2418:STSFAB¿2.0.CO;2

Loder, J. W., Petrie, B. & Gawarkiewicz, G. (1998). The coastal ocean off Northeastern North America: A large-scale view. *This Sea*, *11*, 105–133.

Loder, J. W., & Wang, Z. (2015). Trends and variability of sea surface temperature in the Northwest Atlantic from three historical gridded datasets. *Atmosphere-Ocean*, *53*(5), 510–528. https://doi.org/10.1080/07055900.2015.1071237

Loder, J. W., & Wang, Z. (2024). *Seasonality of trends and modal variability in sea surface temperature in the Northwest Atlantic*. Can. Tech. Rep. Hydrogr. Ocean Sci. 384: vi + 70 p.

Marshall, J., Kushnir, Y., Battisti, D., Chang, P., Czaja, A., Dickson, R., Hurrell, J., McCartney, M., Saravanan, R., & Visbeck, M. (2001). North Atlantic climate variability: Phenomena, impacts and mechanisms. *International Journal of Climatology*, *21*(15), 1863–1898. https://doi.org/10.1002/joc.v21:15

Mills, K., Pershing, A., Brown, C., Chen, Y., Chiang, F.-S., Holland, D., Lehuta, S., Nye, J., Sun, J., Thomas, A., & Wahle, R. (2013). Fisheries management in a changing climate. *Oceanography*, *26*(2), 191–195. https://doi.org/10.5670/oceanog

Moisan, J. R., & Niiler, P. P. (1998). The seasonal heat budget of the North Pacific: Net heat flux and heat storage rates (1950–1990). *Journal of Physical Oceanography*, *28*(3), 401–421. https://doi.org/10.1175/1520-0485(1998)028¡0401:TSHBOT¿2.0.CO;2

O'Carroll, A. G., Eyre, J. R., & Saunders, R. W. (2008). Three-way error analysis between AATSR, AMSR,E, and in situ sea surface temperature observations. *Journal of Atmospheric and Oceanic Technology*, *25*(7), 1197–1207. https://doi.org/10.1175/2007JTECHO542.1

Oliver, E. C. J., Benthuysen, J. A., Darmaraki, S., Donat, M. G., Hobday, J., Holbrook, N. J., Schlegel, R. W., & Sen Gupta, A., (2021). Marine heatwaves. *Annual Review of Marine Science*, *13*(1), 313–342. https://doi.org/10.1146/marine.2021.13.issue-1

Overland, J. E., & Preisendorfer, R. W. (1982). Significance test for principal components applied to a cyclone climatology. *Monthly Weather Review*, *110*(1), 1–4. https://doi.org/10.1175/1520-0493(1982)110¡0001:ASTFPC¿2.0.CO;2

Petrie, B., & Drinkwater, K. (1993). Temperature and salinity variability on the scotian shelf and in the Gulf of Maine 1945–1990. *Journal of Geophysical Research*, *98*(C11), 20079–20089. https://doi.org/10.1029/93JC02191

Rayner, N. A., Parker, D. E., Horton, E. B., Folland, C. K., Alexander, L. V., Rowell, D. P., Kent, E. C., & Kaplan, A. (2003). Global analyses of sea surface temperature, sea ice, and night marine air temperature since the late nineteenth century. *Journal of Geophysical Research D: Atmospheres*, *108*(14), 1–29.

Richaud, B., Kwon, Y. O., Joyce, T. M., Fratantoni, P. S., & Lentz, S. J. (2016). Surface and bottom temperature and salinity climatology along the continental shelf off the Canadian and U.S. East Coasts. *Continental Shelf Research*, *124*, 165–181. https://doi.org/10.1016/j.csr.2016.06.005

Rodgers, K. B., Lee, S. S., Rosenbloom, N., Timmermann, A., Danabasoglu, G., Deser, C., Edwards, J., Kim, J.-E., Simpson, I. R., Stein, K., Stuecker, M. F., Yamaguchi, R., B'odai, T., Chung, E.-S., Huang, L., Kim, W. M., Lamarque, J.-F., Lombardozzi, D. L., Wieder, W. R., & Yeager, S. G., (2021). Ubiquity of human-induced changes in climate variability. *Earth System Dynamics*, *12*(4), 1393–1411.

Roemmich, D., Gilson, J., Willis, J., Sutton, P., & Ridgway, K. (2005). Closing the time-varying mass and heat budgets for large ocean areas: The Tasman Box. *Journal of Climate*, *18*(13), 2330–2343. https://doi.org/10.1175/JCLI3409.1

Shearman, R. K., & Lentz, S. J. (2010). Long-term sea surface temperature variability along the U.S. East Coast. *Journal of Physical Oceanography*, *40*(5), 1004–1017. https://doi.org/10.1175/2009JPO4300.1

Simpson, I. R., Bacmeister, J., Neale, R. B., Hannay, C., Gettelman, A., Garcia, R. R., Lauritzen, P. H., Marsh, D. R., Mills, M. J., Medeiros, B., & Richter, J. H. (2020). An evaluation of the large-scale atmospheric circulation and its variability in CESM2 and other CMIP models. *Journal of Geophysical Research: Atmospheres*, *125*(13), 1–42.

Stevenson, J. W., & Niiler, P. P. (1983). Upper ocean heat budget during the Hawaii-to-Tahiti shuttle experiment. *Journal of Physical Oceanography*, *13*(10), 1894–1907. https://doi.org/10.1175/1520-0485(1983)013¡1894:UOHBDT¿2.0.CO;2

Trenberth, K. E., & Shea, D. J. (2006). Atlantic hurricanes and natural variability in 2005. *Geophysical Research Letters*, *33*(12), 1–4. https://doi.org/10.1029/2006GL026894

Vicente-Serrano, S. M., & López-Moreno, J. I. (2008). Nonstationary influence of the North Atlantic Oscillation on European precipitation. *Journal of Geophysical Research: Atmospheres*, *113*(20), 1–14.

Visbeck, M., Chassignet, E. P., Curry, R. G., Delworth, T. L., Dickson, R. R., & Krahmann, G. (2003). The ocean's response to North Atlantic Oscillation variability. *Geophysical Monograph Series*, *134*, 113–145.

Wills, R. C., Armour, K. C., Battisti, D. S., & Hartmann, D. L. (2019). Ocean-atmosphere dynamical coupling fundamental to the Atlantic multidecadal oscillation. *Journal of Climate*, *32*(1), 251–272. https://doi.org/10.1175/JCLI-D-18-0269.1